Chronology and eccentricity phasing for the Early Turonian greenhouse (~93-94 Ma): constraints on astronomical control of the carbon cycle

Jiří Laurin[1], David Uličný[1], Stanislav Čech[2], Jakub Trubač[3], Jiří Zachariáš[3], Andrea Svobodová[4]

[1] *Institute of Geophysics of the Czech Academy of Sciences, Boční II/1401, 141 31 Prague, Czech Republic*

[2] *Czech Geological Survey, Prague, Czech Republic*

[3] *Institute of Geochemistry, Mineralogy and Mineral Resources, Charles University, Prague, Czech Republic*

[4] *Institute of Geology of the Czech Academy of Sciences, Prague, Czech Republic*

ABSTRACT

The Early Turonian interval represents a unique confluence of climatic and oceanographic conditions including peak surface temperatures, high greenhouse-gas concentrations and maximum Phanerozoic sea level. The susceptibility of this climate mode to short-term forcings such as astronomically paced insolation remains poorly understood partly due to a limited time control and unknown phasing of astronomical cycles in this interval. Here we offer a refined astrochronology of the Early Turonian based on laterally consistent precession signals preserved in offshore strata of the Bohemian Cretaceous Basin (central Europe). Pristine amplitude modulation verified through interference patterns in depth-frequency plots provides a robust indication of ~100-kyr and 405-kyr eccentricity phases (maxima and minima) that are pinned

to ammonite biozones and new carbon-isotope data from two cores. The Early Turonian is estimated as 885 ±46 thousand years (kyr) in duration, with the Cenomanian-Turonian boundary predating the nearest 405-kyr maximum by 81 ±32 kyr. The results support a possible link of the recovery from Oceanic Anoxic Event II to increasing magnitude of seasonal insolation extremes due to rising eccentricity on 405-kyr and million-year (Myr) time scales. Superimposed upon this trend are small-scale carbon-isotope anomalies the pacing of which passes from ~110 kyr, resembling short eccentricity, to ~170-kyr, possibly related to obliquity modulation. The loss of short-eccentricity pacing despite Myr-scale increase in eccentricity amplitudes suggests decoupling of the carbon-cycle perturbations from low-latitude seasonal insolation and involvement of mid- to high-latitude carbon reservoirs.

1. INTRODUCTION

Following a major climatic perturbation related to the Oceanic Anoxic Event II (OAE II; Schlanger and Jenkyns, 1976), the Early Turonian, ~93-94 million years (Myr) ago, was an episode of stabilized climate of what is considered the peak Phanerozoic greenhouse warmth (Clarke and Jenkyns 1999; Friedrich et al. 2012). Both surface temperatures and global sea level reached extreme levels owing primarily to high rates of ocean-crust production and CO_2 outgassing (e.g., Jones and Jenkyns 2001). Compared to OAE II, the carbon-isotope signature is enriched in the isotope ^{12}C suggesting reduced capacity of oceanic and terrestrial organic reservoirs, i.e., improved recycling of organic carbon that likely contributed to radiative forcing of greenhouse gases. Short-term (10s kyr) carbon-isotope anomalies with magnitudes 0.2-0.5 ‰ in both organic and carbonate carbon (Jarvis et al. 2006, 2015; Fig. 1) point to transient perturbations to the carbon cycle of possible Milankovitch origin (Voigt et al. 2007). The Early Turonian thus represents a rare example of peak greenhouse climate, destabilized on short time scales by external forcings. The potential astronomical origin represents a testable hypothesis that can be evaluated with detailed temporal constraints.

Earlier astrochronologies suggested durations of the Early Turonian in the range of 0.78 to 0.84 Myr (Sageman et al. 2006; Voigt et al. 2008; Tab. 1), but a substantial (~20%) disagreement exists between these estimates and the duration provided by the Geological Time Scale 2012 (GTS2012; Gradstein et al. 2012). More recent studies (Sprovieri et al. 2013; Eldrett et al. 2015; Batenburg et al. 2016) provided detailed astronomical contexts including the phases of

orbital eccentricity, but their chronostratigraphy remains controversial (Fig. 1; Tab. 1).

In order to test the published results and provide additional details that might help to better understand the temporal relationships, we present a new astrochronology based on well-preserved precessional and eccentricity signals in the Bohemian Cretaceous Basin. The results offer a robust interpretation of ~100-kyr, 405-kyr and ~2.4-Myr eccentricity phases that provide new insights into the role of astronomical forcing in carbon-cycle perturbations.

2. DEPOSITIONAL SETTING

The Bohemian Cretaceous Basin formed as a continental through shallow-marine siliciclastic system along reactivated, NW-trending faults of the Elbe fault zone (Fig. 2; Uličný et al. 2009). The Cenomanian-Turonian interval is characterized by a basinwide flooding and expansion of hemipelagic carbonates across the basin. The overlying Turonian statigraphy consists predominantly of coarse-grained progradational wedges of deltaic and nearshore siliciclastics (genetic sequences TUR1-3; Uličný et al. 2009) that interfinger distally with offshore to hemipelagic fines (Figs. S1-S6). Astronomical signals are best expressed in distal parts of the siliciclastic depocenter where hemipelagic marlstones and limestones (type A cycles; Figs. 3, S7 and S8) pass upward into offshore through distal prodelta facies with cyclic variations in sand vs. mud contents (highlighted by carbonate cementation; type B cycles; Figs. S7, S8).

3. DATA AND METHODS

3.1. Data

87 This study is based on subsurface data. An extensive borehole and well-log
88 database provides a 3-dimensional stratigraphic framework (Uličný et al., 2009,
89 2014) and makes it possible to (i) trace changes in lithofacies and stratal
90 geometries in the study area to determine the most suitable sites for time series
91 analysis, and (ii) correlate biostratigraphic datums, carbon-isotope events and
92 floating astrochronology across the basin (Figs. S1-S6).
93 All boreholes examined here exhibit long-term changes in sedimentation
94 rate reflecting a long-term progradation of the marginal-marine siliciclastic
95 system and shallowing of the coeval hemipelagic setting. Shorter-term
96 fluctuations in sedimentation rates related to non-deposition and/or erosion
97 across syndepositional faults are documented locally by angular relationships of
98 well-log correlation markers (Figs. S1, S2). Boreholes suitable for time-series
99 analysis and the construction of astronomical age model were selected from the
100 prodeltaic zone based on two criteria: (i) The long-term change in sedimentation
101 rate follows a simple pattern that can be modeled and removed numerically (e.g.,
102 linear change in sedimentation rate matched by a reciprocal function of signal
103 wavelength in the depth-frequency plot; Fig. 4b). (ii) Short-term hiatuses and
104 other fluctuations in sedimentation rates are absent or short relative to the
105 tuning targets. The closest fit to these criteria is found in borehole J-719670
106 located ~5 km offshore from the progradational limit of sequence TUR2 (Fig. 2).
107 Complementary analyses were executed on a series of other boreholes from the
108 along-dip correlation profile. The list of key boreholes, their geographic
109 coordinates and types of data are provided in Table S1.
110 Time-series analysis (section 3.4) was applied primarily to high-
111 resolution resistivity logs that serve as a proxy for variations in sand/mud ratio

and carbonate cementation. The LL7 focused laterolog probe offers a favorable combination of sensitivity to dm- to meter-scale lithological variations in the mixed carbonate-siliciclastic strata, and noise attenuation (gamma-ray logs appear excessively noisy at the dm to meter scales as revealed by comparing closely spaced boreholes). The depth resolution of digitized resistivity logs is 10 cm, which in the reference borehole J-719670 corresponds to a minimum of 10 samples per the shortest (precessional) cycle discussed in this paper.

Isolated core samples from two boreholes (J-703684 and J-854604) and complete cores from boreholes 4523-A Sedlec and 4530-A Horní Beřkovice (Fig. 3) were available for a detailed examination of lithology and geochemistry. Greyscale-density profiles for the 4523-A Sedlec core were extracted from high-resolution (~10 pixels/mm) photographs using the image-processing software ImageJ (National Institutes of Health, Bethesda, MD).

3.2. Geochemistry

Samples from the 4523-A Sedlec and 4530-A Horní Beřkovice cores were analyzed for carbon-isotope composition of bulk organic carbon ($\delta^{13}C_{org}$). The measurements were performed in the Stable Isotope Laboratory of the Geological Survey, Prague (4523-A), and the Institute of Geochemistry, Mineralogy and Mineral Resources, Charles University, Prague (4530-A). Samples (10-15 g) were pulverized to an analytical-grade powder and decalcified using 10% HCl. Additional details are provided in Text S1. Data are reported relative to the Vienna Peedee Belemnite (VPDB) standard. Reproducibility of duplicate measurements was 0.12 ±0.08 (1σ) ‰ VPDB. The

temporal resolution of $\delta^{13}C_{org}$ data from the core 4523-A is 6.7 ±4.6 (1σ) kyr, according to the age model presented here.

Major and trace element concentrations were measured with an XRF spectrometer NITON XL3t GOLDD+; the XRF output was calibrated using 10 samples analyzed in an accredited laboratory of the Nanotechnology Centre, Technical University of Ostrava.

3.3. Chronostratigraphy, biostratigraphy

The Cenomanian/Turonian (C/T) boundary is constrained by a carbon-isotope correlation to the USGS #1 Portland core (Fig. S13) and well-log correlation of the base of ammonite Zone *Watinoceras devonense* from the Pecínov section, indicated there by the occurrence of inoceramid bivalve *Mytiloides puebloensis* (Fig. S4; cf. Košťák et al., 2018). The Lower Turonian ammonite Zone *Mammites nodosoides* is delineated by FO *M. nodosoides* at Pecínov (Košťák et al. 2018); a relatively large uncertainty in the correlation FO *M. nodosoides* and *W. devonense* to borehole 4523-A Sedlec (Fig. 3) is due to stratigraphic condensation at Pecínov (Figs. S4 and S13). The base of nannofossil Zone UC 7 which correlates above the base of the *M. nodosoides* Zone (Burnett 1998) is identified at approximately 178.75-181.75 m depth of the core 4523-A (Text S2). The first occurrence of the ammonite *Collignoniceras woollgari* (Mantell), which marks the Lower/Middle Turonian boundary (Gradstein et al. 2012), is correlated from borehole Nm-1 (Figs. S5, S6). The base of the Middle Turonian is further confirmed by the Lulworth carbon-isotope excursion (Jarvis et al. 2006; Fig. 1) identified in boreholes 4523-A and 4530-A (Fig. 3).

3.4. Time-series analysis and signal processing

Spectral estimates are calculated with the multitaper method (MTM; Thomson 1982) and evolutive harmonic analysis (EHA; Meyers et al. 2001). The statistical significance of the spectral results is quantified using the MTM harmonic F-test (Thomson 1982), and the assignment of spectral maxima to precessional, obliquity and eccentricity terms is verified with the Average Spectral Misfit (ASM; Meyers and Sageman 2007). Frequencies of orbital eccentricity for ASM analysis are estimated from the solutions La2010a through La2010d (Laskar et al. 2011a) following the approach of Malinverno et al. (2010) and Meyers et al. (2012b). Precessional and obliquity frequencies for ASM analysis are adopted from Waltham (2015). All ASM parameters are listed in Tables S2a and S2b. The TimeOpt method (Meyers 2015) is used to verify the correlation between the eccentricity signal and precessional envelope in selected intervals (Figs. S10, S11). All spectral estimates, ASM and TimeOpt calculations are conducted using the R package 'Astrochron', version 0.6 (Meyers, 2014; R Core Team, 2015). Signal filtering is performed with the Matlab script EPNOSE (Laurin et al. 2017) using a modification of the Taner filter (Taner 1992), which is symmetrical on a linear scale (Kodama and Hinnov 2014). Modulation envelopes were extracted with the Hilbert transform in the Matlab Signal Processing Toolbox; the algorithm is based on Marple (1999).

Data preparation included removal of a large-scale linear trend in sedimentation rate. This trend is manifested as a systematic drift in amplitude and F-test significance maxima approximating a reciprocal function of signal wavelength in the frequency domain (Figs. 4b and S9). To remove the linear trend, the depth scale of borehole J-719670 was modified by considering that the

mean spatial period of the precessional cycle evolved linearly from 1/1.05 m at the depth of 403 m to 1/0.32 m at the depth of 368 m (Fig. 4b), and setting this path to a constant value of 1/1.05 m (Fig. 4c). An analogous adjustment is applied to borehole J-650704, where a linear change from the period of 1/1.01 m at the depth of 428 m to the period of 1/0.35 m at the depth of 395 m is tuned to a constant period of 1/1.01 m. The resulting vertical scales are referred to as "detrended depth scales" in this paper (Figs. 4 and 5). Importantly, this type of linear pre-tuning is applied to an interval the time span of which greatly exceeds the period of short-eccentricity cycles (>300 kyr) and therefore should not distort the ~100-kyr modulation patterns examined in this study (section 4.2; cf. Zeeden et al. 2015). In order to reduce variance in the carbonate-rich interval of type A cyclicity, resistivity logs were converted to their common logarithm prior to time-series analysis. Additional details are provided in sections 4.1 through 4.4.

3.5 Astronomical solutions

Precessional and eccentricity signatures identified in this study are compared primarily with the astronomical solution La2010d (Laskar et al. 2011a), because this solution provides the most recent estimate for the precessional index (note that later solutions – Laskar et al. 2011b; Zeebe 2017; Zeebe and Lourens 2019 – are limited to eccentricity). The La2010d reconstructions of precessional index and obliquity have been obtained following the procedure described in Wu et al. (2013). We note, however, that all solutions available to date are unreliable in their prediction of Myr-scale eccentricity modulation beyond ~55 Myr ago (Laskar et al. 2011b; Zeebe 2017; Zeebe and Lourens 2019). No attempt is

211 therefore made in this study to pin the study interval to any particular segment
212 of the astronomical solution. The La2010d series is used primarily as a
213 constraint for the astronomical tuning target and its uncertainty. The solution
214 La2004 (Laskar et al. 2004) is shown for comparison, because, unlike La2010d, it
215 offers compatible eccentricity phases within the bounds of radioisotopic
216 uncertainty (±0.15 Myr, Meyers et al. 2012a) and provides the closes fit to Myr-
217 scale modulation in the Turonian interval (Ma et al. 2019).
218
219 **3.6 Age model**
220 Astrochronology is based on precessional and eccentricity signals identified in
221 the study interval. To estimate the uncertainty related to unstable astronomical
222 solutions, the interpreted precessional cycles are correlated to all segments of
223 the solution La2010d (Laskar et al., 2011a) between 89 and 99 Myr ago that are
224 compatible with eccentricity phasing in the study interval. Interpolation of the
225 age-depth relationships is based on the Bayesian approach and executed with
226 Bchron (Haslett and Parnell 2008). Further details are provided in section 4.4.
227
228 **3.7 Terminology**
229 The term "phasing" is used in this paper to refer to the timing of maxima and
230 minima of astronomical signals. An attempt is made to distinguish the phasing of
231 the original astronomical forcing from the phasing of filtered lithological or
232 geochemical proxies of the astronomical forcing (through amplitude modulation
233 and interference patterns of precessional signals).
234 In a previous study, Laurin et al. (2016) use the term frequency
235 modulation (FM) to describe systematic changes in the frequency of

236 astronomical signals in depth-frequency plots (EHA). Although the EHA patterns
237 discussed here are analogous to Laurin et al.'s FM, a different term – interference
238 patterns (IP) - is used here to avoid confusion with FM examined by other
239 techniques (e.g., Liu et al. 1998; Hinnov 2000).
240
241 **4. RESULTS**
242 **4.1. Astronomical signatures**
243 Spectral estimates and interpretation of astronomical signatures focus on three
244 reference boreholes: J-719670, J-650704, and 4523-A (see Methods; Fig. 3).
245 Borehole J-719670 provides a well-preserved record for most of the Lower
246 Turonian, and is therefore considered the primary reference section. Results for
247 the lower and upper parts of the study interval are refined using data from
248 boreholes 4523-A and J-650704.
249
250 ***4.1.1. Borehole J-719670, resistivity***
251 Spectral estimates for a downhole resistivity log of this borehole show distinct
252 power-spectral and F-test significance maxima in the astronomical band (Fig. 4).
253 Power maxima exceeding the 90% significance level are labelled informally S_1
254 through S_4 and further discussed. A prominent cyclicity starts approximately 5 m
255 beneath the C/T boundary, with most variance located in the frequency band
256 ~0.25 cycle/m (~4 m period; S_2 in Fig. 4). Approximately 6 m above the C/T
257 boundary, the S_2 signal starts fading and the variance is transferred to higher
258 frequencies, namely S_4. This apparent increase in signal resolution follows
259 decreasing carbonate contents and the onset of siliciclastic-dominated (type B)
260 cyclicity that has a distinct response in the resistivity log. A refined, S_4-scale

resolution for the C/T boundary interval is obtained from greyscale data from borehole 4523-A (section 4.1.3).

Further up-section, with an increase in siliciclastic contents related to progradation of sequence TUR2, the S_4 trace in EHA plot drifts to lower frequencies consistent with a linear increase in sedimentation rate (reciprocal function of signal wavelength). Removal of the trend (explained in section 3.4 and Fig. 4b) makes it possible to examine the detailed structure of the S_4 band; the signal is composed of two separate frequencies (labeled S_{4a} and S_{4b}) whose interference is coherent with the S_2 cyclicity (Figs. 4, 5). ASM analysis (Fig. 4d) suggests that the S_2 and S_4 signals correspond to cycles of orbital eccentricity (97-127 kyr; related to g_4-g_5 and g_4-g_2) and climatic precession (~19–23 kyr), respectively. The S_{4a} and S_{4b} components then correspond to the ~23-kyr (k+g_5 and k+g_2) and ~19-kyr (k+g_4 and k+g_3) terms of the precessional index, respectively (where k refers to Earth's precession rate, and g_2 through g_5 are the secular frequencies of planetary motion; Berger and Loutre 1990). A signature of axial obliquity (S_3) is relatively weak and localized; where present, its variance never exceeds variance of the precessional signal (variance ratio <0.7).

The EHA signatures (IP in Figs. 4 and 5) suggest well-preserved precessional and eccentricity signals throughout most of the Lower Turonian. Above the Lower/Middle Turonian boundary, however, the astronomical signals become less distinct at the J-719670 site. In addition, the lowermost Turonian of J-719670 exhibits minor condensation spanning marker bed 9 and corresponding to one S_4 (precessional) cycle (Fig. S1). To confirm and refine the estimate of astronomical cyclicity in these intervals, additional boreholes are examined.

286

287 ***4.1.2. Borehole J-650704, resistivity***

288 This borehole is located approximately 4 km eastward of J-719670, closer to the
289 main siliciclastic depocenter of the Turonian depositional system (Fig. 2).
290 Proximity to the sediment source provides suitable conditions for the extension
291 of the S_4 signal into the Middle Turonian (Fig. 3). Spectral estimates for the
292 resistivity log reveal a pattern of S_2 and S_4 cyclicity, which is compatible with the
293 results for borehole J-719670 (Fig. 5).

294

295 ***4.1.3. Borehole 4523-A, greyscale***

296 Borehole 4523-A Sedlec is located down the depositional dip relative to
297 boreholes J-719670 and J-650704 (Fig. 2). Type B cyclicity, which consists
298 primarily of sand/mud alternations (Figs. S7, S8), is less well expressed in this
299 distal area due to reduced textural variability and local winnowing. However,
300 unlike resistivity logs of J-719670 and J-650704, the high-resolution greyscale
301 record of 4323-A makes it possible to resolve the S_4 signal in carbonate-rich
302 facies surrounding the C/T boundary (Fig. 6).

303

304 **4.2. Eccentricity phasing**

305 The initial information on the phasing of ~100-kyr and 405-kyr eccentricity
306 cycles is obtained from bandpassed resistivity logs following removal of a linear
307 trend in sedimentation rate (Fig. 5). The bandpassed proxy, however, does not
308 bear any information on the polarity of the astronomical term. To estimate the
309 phase of the filtered proxy relative to the phase of the eccentricity forcing, we
310 employ a suit of additional indices including (i) amplitude modulation of

311 bandpassed precessional signal (see section 4.2.1), and (ii) preservation of
312 interference patterns of the precessional signals in depth-frequency plots.
313 Details on the interpretation are given below.
314
315 ***4.2.1. Short eccentricity (~100-kyr)***
316 The inherent role of orbital eccentricity (e) in the climatic impact of axial
317 precession, quantified by the precessional index (e sinω, where ω is the
318 longitude of the perihelion from the moving equinox), results in an eccentricity-
319 paced modulation of the amplitude of precessional signals (e.g., Berger and
320 Loutre 1991). This amplitude modulation has therefore been acknowledged as a
321 tool to identify eccentricity maxima and minima (e.g., Herbert 1992; Grippo et al.
322 2004; Zeebe et al. 2017; Laurin et al. 2017). Any signals filtered from geological
323 data are, however, prone to distortion due to sedimentation-rate instabilities and
324 introduction of noise (both natural and analytical) into the filtered bandwidth.
325 An accurate extraction of amplitude-modulated signals from stratigraphic data
326 involves additional challenges such as frequency leakage out of the filtered
327 bandwidth or introduction of harmonic tones into the filtered bandwidth due to
328 short-term fluctuations in accumulation rates, diagenesis or differential
329 compaction. The use of amplitude modulation therefore requires additional
330 support. Here, the integrity of the precessional envelope is evaluated using
331 interference patterns in EHA plot, analogous to the evaluation of 400-kyr phase
332 in a previous study (Laurin et al. 2016).
333 The composition of fundamental frequencies of the main terms of short-
334 eccentricity (g_4-g_2 and g_4-g_5) and precessional index (k+g_5, k+g_2, k+g_4 and k+g_3;
335 Berger and Loutre 1990) links the interference of precessional terms to the

eccentricity phase, i.e., $(k+g_4)-(k+g_2) = g_4-g_2$, and $(k+g_4)-(k+g_5) = g_4-g_5$. As illustrated in Figure 5c, intervals of constructive interference of the ~19-kyr and ~23-kyr terms mark short-eccentricity maxima, and intervals of destructive interference are aligned with short-eccentricity minima. These patterns can be examined in EHA plots that also make it possible to identify non-stationarities and determine noise levels in the precessional band (see Laurin et al. 2016 for illustration of possible modes of signal distortion and their EHA signatures).

In the resistivity log of J-719670, the interference patterns are well preserved between correlation markers 10 and 37 (Fig. 4) suggesting that the precessional signal and its amplitude modulation are not severely distorted in this interval. The precessional envelope in J-719670 can also be extended some distance beneath a minor hiatus near marker bed 9. The J-650704 record is noisier, but exhibits interference patterns that are consistent with those in J-719670 (Fig. 5). The amplitude envelope of S_4 signal in J-719670 is therefore used in this study as the primary tool for the interpretation of short-eccentricity maxima and minima. For intervals lacking a robust precessional modulation, such as the Cenomanian/Turonian boundary interval, the short eccentricity phases are estimated from a filtered S_2 signal, the polarity of which is confirmed with the TimeOpt analysis (Figs. S10 and S11).

It should be noted that the above approach cannot resolve minor phase differences and deformations that are to be expected in this depositional setting. However, the method of astrochronological tuning applied here (section 4.4) is not sensitive to minor lead/lag differences in the precessional and eccentricity records; the phasing uncertainty is accommodated by the total uncertainty of the age model.

361

362 ***4.2.2. Long eccentricity (405-kyr)***

363 The 405-kyr cycle, the rhythm of which is represented by signal S_1 (Fig. 4d), is
364 part of the same astronomical forcing as the ~100-kyr eccentricity term. The
365 preservation of its polarity should therefore be analogous to the preservation of
366 short-eccentricity phasing inferred in section 4.2.1. This means that maxima in
367 the filtered resistivity log should *approximate* the maxima in the original signal
368 (as noted above, minor phase uncertainties are accommodated by the tuning
369 approach). If so, then 405-kyr maxima should be located near marker beds 2a, 20
370 and 36 (Fig. 5). Support for this assumption can be sought in the modulation of
371 precessional and short-eccentricity signals.

372 As with the short-eccentricity phasing, the phase of 405-kyr eccentricity
373 (g_2-g_5) is involved in the interference of precessional terms. In this case, however,
374 the interpretation in real stratigraphic data would require an exceptionally clear
375 signal permitting separation of the 23.05-kyr (k+g_5) and ~21.81-kyr (k+g_2)
376 precessional terms (Tab. S2a). In spite of an excellent signal preservation, these
377 components cannot be resolved in the study interval. Other indices are therefore
378 required.

379 Pronounced amplitude modulation and well-developed interference
380 patterns in the precessional band can be expected to form preferably during
381 405-kyr maxima, as in the theoretical solutions. The nodes in 405-kyr
382 eccentricity, in contrast, should exhibit relatively weak precessional signals and
383 indistinct interference patterns in time-frequency plots (Fig. 5c). Following these
384 assumptions, 405-kyr maxima should be centered between marker beds 17 – 21
385 and near markers 36 – 37, in agreement with the S_1 bandpass (Fig. 5a,b). This

386 interpretation is further supported by a transient record of eccentricity in the
387 Lower/Middle Turonian boundary interval in borehole Bch-1 (central part of the
388 basin; Figs. 7a and S12).

389 Modulation of the short-eccentricity signal (S_2) is of limited use due to an
390 upward decline in its power. Gradual facies change above marker bed 2b (Fig.
391 S7) and local winnowing of marker bed 9 (Fig. 5) also corrupt the S_1 bandpass in
392 the lower part of the study interval. To preserve a realistic, ~1:4 bundling of
393 short-eccentricity vs. long-eccentricity cycles, the lowermost maximum of the
394 405-kyr eccentricity should be located some distance above the lowermost
395 maximum of the S_1 bandpass, between markers 2b and 3 (between short-
396 eccentricity maxima ecc2 and ecc3; Figs. 5 and 7).

397 The final support for the interpretation of 405-kyr phase comes from
398 bundling ratios of short-eccentricity vs. precessional cycles that are controlled
399 chiefly by changes in the instantaneous period of short-eccentricity cycles. The
400 405-kyr minima are typically associated with low instantaneous periods (as low
401 as 77 kyr; Hinnov 2000) and low bundling ratios (as low as 1:3 during ~2.4-Myr
402 nodes). In the study interval, the bundling ratios range from 3.5 to 5.7 with
403 minima near marker beds 7 and 31, coincident with 405-kyr minima predicted
404 by the S_1 bandpass and precessional interference patterns (Fig. 7).
405

406 **4.3. Myr-scale eccentricity**

407 The ~2.4-Myr modulation of orbital eccentricity related to the precession of
408 perihelia of Earth and Mars ($g_4 - g_3$; Laskar et al. 2004) cannot be interpreted
409 directly due to a relatively short time span of the study interval (~1 Myr).
410 However, since long-term eccentricity minima exhibit suppressed ~100-kyr

411 modulations (Fig. 5c; cf. Hinnov 2000), the exquisite preservation of ~100-kyr
412 interference patterns in the middle part of the Lower Turonian and lower part of
413 the Middle Turonian makes it possible to infer a broadly defined ~2.4-Myr
414 maximum in this interval. Such a phasing implies a ~2.4-Myr node overlapping
415 with OAE II, in agreement with the results of previous studies (Batenburg et al.
416 2016; Laurin et al. 2016; Ma et al. 2019).
417
418 **4.4 Age model**
419 The study interval spans twelve short-eccentricity cycles labelled ecc1 through
420 ecc11 (a minor cycle at 405-kyr minimum is labelled ecc3b; Fig. 7). These cycles,
421 combined with the precessional cyclicity, provide the basis for the construction
422 of floating age model. The key issue affecting accuracy of the age estimate is the
423 selection of tuning targets for the eccentricity and precessional signals. A
424 constant tuning target, e.g., 95 kyr for short eccentricity, can be considered
425 inaccurate, because the instantaneous period of this cycle varies significantly in
426 the course of 405-kyr and Myr-scale modulations (e.g., Hinnov 2000). Tuning to a
427 particular segment of an astronomical solution would settle this issue, but all
428 astronomical solutions available to date are unreliable in their prediction of Myr-
429 scale eccentricity modulation beyond ~55 Myr ago (Laskar et al. 2011a,b; Zeebe
430 2017; Zeebe and Lourens 2019). To estimate the uncertainty associated with
431 Myr-scale modulation, we select a 10-Myr interval of the solution La2010d
432 centered at 94 Myr ago (~C/T boundary) and tune the observed signals to every
433 compatible segment of the theoretical solution in this interval.
434 The tuning is performed by linking individual S_4 cycles with precessional
435 cycles of the La2010d solution (Laskar et al. 2011a) within the framework of

436 ~100-kyr (S_2) and 405-kyr (S_1) maxima and minima interpreted in section 4.2. In
437 this concept, the precessional cycles provide the temporal resolution and
438 eccentricity cycles provide stability (by, for example, identifying missing
439 precessional beats at eccentricity minima). Each tuning assigns floating ages to
440 correlation markers 1 through 43, which are manifestations of the precessional
441 (S_4) cyclicity (Figs. S14 and S15). The mean and standard deviation of the
442 floating ages, calculated from the total number of tuned segments (n=21),
443 constitute the nominal age model and uncertainty of the tuning target (Tab. S3).
444 An interpolation of the nominal age model to chronostratigraphic
445 boundaries using the Bayesian approach (Bchron; Haslett and Parnell 2008)
446 suggests an 885 kyr duration for the Early Turonian. The uncertainty of this time
447 span is estimated as ±46 kyr (95% confidence interval) by combining the
448 uncertainty of the location of chronostratigraphic boundaries (Fig. 3) and the
449 uncertainty of the La2010d tuning target (Tab. 2). The age model makes it
450 possible to define the mean floating ages and uncertainties for the ~100-kyr and
451 405-kyr maxima and minima (Fig. 8): the Cenomanian/Turonian boundary
452 predates the nearest 405-kyr maximum by 81 ±32 kyr, and the Lower/Middle
453 Turonian boundary coincides with another 405-kyr maximum within the
454 uncertainty of ±33 kyr.
455
456 **4.5 Age-calibrated $\delta^{13}C$**
457 The Bayesian interpolation is further applied to estimate floating ages of carbon-
458 isotope samples in borehole 4523-A (Fig. 8). This age calibration suggests that
459 the negative shift in $\delta^{13}C$ following OAE II is superimposed upon increasing 405-
460 kyr eccentricity. The temporal distribution of small-scale anomalies

approximates a ~110-kyr pacing in the lowermost Turonian, but passes to a longer, ~170-kyr pattern towards the Middle Turonian (Fig. 8d).

5. DISCUSSION

5.1 Chronology of the Early Turonian

The floating-age estimate presented here falls within the range presented in previous studies (Tab. 1). It is most closely compatible with astrochronology of the Wunstorf core (Voigt et al. 2008), with which it shares the precession-scale resolution. The minor difference in the duration of Early Turonian (~40 kyr) between these models might be related to the selection of monochromatic precessional tuning target (21 kyr) and the loss of precessional signal in the uppermost part of the Lower Turonian at Wunstorf. Another robust estimate, the Portland time scale of Meyers et al. (2001, 2012a) and Sageman et al. (2006), appears ~100 kyr short compared to the Bohemian model. The difference is again possibly related to the use of a monochromatic tuning target, in this case the 95 kyr for short eccentricity in Portland (note that the use of mean short-eccentricity period of 110 kyr would increase the duration estimate by 16%, matching the Bohemian estimate within its uncertainty). Other published astrochronologies are difficult to assess due uncertainties in the definition of chronostratigraphic boundaries in the Bottaccione (Sprovieri et al. 2013), Contessa (Batenburg et al. 2016) and Iona (Eldrett et al. 2015) records.

5.2 Eccentricity phasing across OAE II

The inferred ~2.4-Myr node in eccentricity modulation during OAE II and a long-term increase in the eccentricity amplitudes towards the Middle Turonian are in

agreement with previous results supporting the role of increasing seasonality in the recovery from OAE II (Batenburg et al. 2016; Laurin et al. 2016). The 405-kyr phasing, in contrast, cannot be compared directly with previous studies due to uncertainties in stratigraphic correlation to published sections (Figs. 1 and S17) and a lack of direct phase constraints across OAE II. Well-preserved astronomical signals allowing a robust interpretation of the 405-kyr phases have been described from the pre-OAE II interval at Furlo (Batenburg et al. 2016; Laurin et al. 2016). When extrapolating eccentricity cycles of the Bohemian record to the base of OAE II using published astrochronologies (Sageman et al. 2006; Ma et al. 2014; Fig. S13), the 405-kyr maxima appear ~90 kyr (80°) out-of-phase relative to the Furlo record (Fig. 8c). Considering that both the Early Turonian and pre-OAE II eccentricity records are robust, the most likely source of error is in the extrapolation across OAE II. Possible explanations of the misfit include non-deposition or condensation near the base of Livello Bonarelli at Furlo, or a minor underestimation of the period of the eccentricity tuning target in the OAE II chronology (since the 95 kyr target used in the Portland astrochronology is at the low range of eccentricity periods; see also section 5.1).

Another apparent misfit is found in the Early Turonian, when comparing the Bohemian 405-kyr record with eccentricity maxima inferred for the Contessa section (Batenburg et al. 2016; Figs. 1f and S17). The two records can, however, be aligned with each other when considering a ±150 kyr uncertainty for the Contessa section (Batenburg et al. 2016) and delineating the Cenomanian/Turonian boundary as in Wendler (2013) (Fig. S17).

5.3 Short-term $\delta^{13}C$ anomalies: interbasinal correlation

511 To facilitate the comparison of different records, we offer a simple adjustment of
512 the English Chalk and Portland $\delta^{13}C$ curves based on linear interpolation
513 between the C/T boundary and the newly proposed floating age of the
514 Lower/Middle Turonian boundary (Fig. 8). This simplified approach suggests
515 that the Holywell CIE (Jarvis et al. 2006) postdates the C/T boundary by 300-400
516 kyr and might be correlative to the excursion Tu2 or a minor anomaly above Tu1
517 at Wunstorf (supported by the first occurrence of *M. nodosoides* immediately
518 above Tu2; Fig. 8; cf. Voigt et al. 2008). In the Bohemian Cretaceous Basin, the
519 most likely candidate for the Holywell CIE is the excursion "se-10".
520 In general, a correlation of small-scale CIEs that lack a distinct structure
521 or magnitude will remain ambiguous without biostratigraphic constraints or
522 detailed age calibration of both the reference section and the correlated section.
523 The original depth-domain profiles and time-domain profiles interpolated across
524 large intervals can provide misleading information about the relative spacing of
525 CIEs due to unrecognized changes in sedimentation rates and distorted age-
526 depth relationships.
527
528 **5.4 Short-term $\delta^{13}C$ anomalies: timing and origin**
529 The ~100-kyr recurrence interval of short-term $\delta^{13}C$ anomalies in the earliest
530 Turonian (Fig. 8) points to the possible influence of eccentricity-modulated
531 seasonal insolation intensities on the carbon-cycle budget (cf. Berger et al. 1993).
532 The $\delta^{13}C$ signature is, however, not strictly coherent with inferred short-
533 eccentricity cycles (Fig. 6) suggesting a causal mechanism different from that
534 proposed for other greenhouse intervals, e.g., Paleocene-Eocene (Cramer et al.
535 2003; Zeebe et al. 2017). The observed incoherency may point to the

536 heterogeneous composition of carbon sources and sinks, involving sensitivity to
537 different aspects of the insolation control (e.g., seasonal intensity vs. integrated
538 seasonal insolation) and geographic locations. The possible role of high- or mid-
539 latitude carbon reservoirs responding to meridional insolation gradients (cf.
540 Raymo and Nisancioglu 2003) or integrated summer insolation (cf. Huybers
541 2006) is apparent in the transition towards ~170-kyr pacing of $\delta^{13}C$ anomalies in
542 the mid Early Turonian (Fig. 8d). The ~170-kyr term occurs in amplitude
543 modulation of axial obliquity (Hinnov 2000; Fig. S16) and its record in the
544 isotopic balance of the carbon cycle can be amplified by the ~100-kyr residence
545 time of carbon (Kump and Arthur 1999), analogous to the amplification of
546 eccentricity terms from precessional modulation (e.g., Short et al. 1991; Herbert
547 1997).

548 Notably, the transition from short-eccentricity pacing to ~170-kyr pacing
549 is superimposed upon the rising phase of long-term eccentricity modulation
550 (Figs. 5 and 8b). The loss of eccentricity pacing of $\delta^{13}C$ excursions can therefore
551 not be attributed to the inherent change in eccentricity amplitudes. To produce
552 the observed pattern, the carbon-cycle perturbations must have decoupled from
553 low-latitude seasonal insolation involving carbon storage in the monsoonal belt
554 (cf. Rossignol-Stricks 1983). The lead control on carbon-isotope mass balance
555 was transferred to mid- to high-latitudes during this interval, paralleling a Myr-
556 scale, obliquity-paced carbon exchange inferred in previous studies (Wendler et
557 al. 2014; Laurin et al. 2015) and the onset of long-term cooling of surface
558 temperatures (cf. Pucéat et al. 2003; Friedrich et al. 2012).

559

560 **SUMMARY**

1. The record of precessional and eccentricity cycles in the Bohemian Cretaceous Basin constrains the duration of Early Turonian to 885 ±46 kyr.
2. The Cenomanian/Turonian boundary precedes the nearest 405-kyr maximum by 81 ±32 kyr. The recovery from OAE II is superimposed upon rising phases of 405-kyr and ~2.4-Myr eccentricity. The ~2.4-Myr cycle peaks between late Early Turonian and early Middle Turonian.
3. Astronomical control on the post-OAE II carbon cycle is documented by ~110-kyr pacing of $\delta^{13}C$ anomalies, which gives way to ~170-kyr obliquity pattern during the mid Early Turonian. The transition suggests decoupling of the carbon-cycle mass balance from low-latitude seasonal insolation and increasing role of high latitude carbon reservoirs.
4. The temporal and phasing constraints presented in this study can facilitate evaluation of short-term climate controls during peak greenhouse conditions.

ACKNOWLEDGMENTS

This research was supported by the Czech Science Foundation (GAČR) project No. 17-10982S, research program RVO 67985530 of the Czech Academy of Sciences of the Czech Republic, and research program RVO 67985831 of the Czech Geological Survey. Acquisition of digital well-log data and core samples was made possible through cooperation with DIAMO, s.p. and the Czech Geological Survey. We are particularly grateful for help with data acquisition to Roland Nádaskay, Jaroslav Valečka, Pavel Veselý, and Dana Čápová. Lukáš Hronec assisted with core preparation and sampling. Comments by Silke Voigt, David De

586 Vleeschouwer, and an anonymous reviewer helped considerably to improve the
587 first version of this paper.

588

589 **DATA AVAILABILITY**

590 Data discussed in this paper are provided in the Supplementary Information,
591 Datasets S1 through S5. By the time this article is accepted for publication, all
592 data will be deposited in the Pangaea Data Publisher.

593 **REFERENCES**

594 Batenburg, S. J., D. De Vleeschouwer, M. Sprovieri, F. J. Hilgen, A. S. Gale, B. S.
595 Singer, C. Koeberl, R. Coccioni, P. Claeys, and A. Montanari (2016), Orbital
596 control on the timing of oceanic anoxia in the Late Cretaceous. Clim. Past,
597 12, 1995-2009, doi:10.5194/cp-12-1995-2016.

598 Berger, A.., and M. F. Loutre (1990), Origine des fréquences des éléments
599 astronomiques intervenant dans le calcul de l'insolation. Bulletin de la
600 Classe des sciences, tome 1. pp. 45-106, doi:10.3406/barb.1990.38523

601 Berger, A., and M. F. Loutre (1991), Insolation values for the climate of the last 10
602 million years, Quat. Sci. Rev. 10, 297–317.

603 Berger, A., M. F. Loutre, and C. Tricot (1993), Insolation and Earth's orbital
604 periods. Journal of Geophysical Research, 98 (D6), 10,341–10,362,
605 doi:10.1029/93JD00222.

606 Burnett, J.A. (1998), Upper Cretaceous. In: Calcareous Nannofossil
607 Biostratigraphy (P.R. Bown), 132–199. British Micropalaeontological
608 Society, London.

609 Čech, S., V. Klein, J. Kříž, and J. Valečka (1980), Revision of the Upper Cretaceous
610 stratigraphy of the Bohemian Cretaceous Basin, Věst. Ústřed. Úst. Geol.
611 (Bull. Geol. Surv. Prague), 55, 277–296.

612 Clarke, L. J., and H. C. Jenkyns (1999), New oxygen isotope evidence for long-term
613 Cretaceous climatic change in the Southern Hemisphere, Geology, 27,
614 699–702, doi:10.1130/0091-7613(1999)027<0699:NOIEFL>2.3.CO;2.

615 Cramer, B. S., J. D. Wright, D. V. Kent, and M. P. Aubry (2003), Orbital climate
616 forcing of $\delta^{13}C$ excursions in the late Paleocene–early Eocene (chrons
617 C24n–C25n), Paleoceanography, 18, 1097, doi:10.1029/2003PA000909.

618 Du Vivier, A. D. C., D. Selby, B. B. Sageman, I. Jarvis, D. R. Gröcke, and S. Voigt, S.
619 (2014), Marine $^{187}Os/^{188}Os$ isotope stratigraphy reveals the interaction of
620 volcanism and ocean circulation during Oceanic Anoxic Event 2, Earth
621 Planet. Sc. Lett., 389, 23-33, doi:10.1016/j.epsl.2013.12.024.
622 Eldrett, J.S., Ma, C., Bergman, S.C., Lutz, B., Gregory, F.J., Dodsworth, P., Phipps, M.,
623 Hardas, P., Minisini, D., Ozkan, A., Ramezani, J., Bowring, S.A., Kamo, S.L.,
624 Ferguson, K., Macaulay, C., and Kelly, A.E. (2015), An astronomically
625 calibrated stratigraphy of the Cenomanian, Turonian and earliest
626 Coniacian from the Cretaceous Western Interior Seaway, USA: Im-
627 plications for global chronostratigraphy. Cretaceous Research, v. 56, p.
628 316–344, https://doi.org/10.1016/j.cretres.2015.04.010.
629 Friedrich, O., R. D. Norris, and J. Erbacher (2012), Evolution of middle to Late
630 Cretaceous oceans—A 55 m.y. record of Earth's temperature and carbon
631 cycle, Geology, 40, 107–110, doi:10.1130/G32701.1.
632 Gradstein, F.M., Ogg, J.G., Schmitz, M. and Ogg, G. (2012), The Geologic Time Scale:
633 Elsevier, 1144 p.
634 Grippo, A., Fischer, A.G., Hinnov, L.A., Herbert, T.D., Premoli Silva, I. (2004),
635 Cyclostratigraphy and chronolo- gy of the Albian stage (Piobbico Italy). In:
636 D'Argenio, B. et al. (Eds.), Cyclostratigraphy: Approaches and Case
637 Histories. Special Publication SEPM (Society for Sedi- mentary Geology)
638 81, 57–81.
639 Hinnov, L.A. (2000), New perspectives on orbitally forced stratigraphy: Annual
640 Review of Earth and Planetary Sciences, 28, 419–475.

641 Haslett, J., & Parnell, A. (2008), A simple monotone process with application to
642 radiocarbon-dated depth chronologies. Journal of the Royal Statistical
643 Society: Series C (Applied Statistics), 57(4), 399–418.
644 Hay, W. W., R. M. DeConto, C. N. Wold, K. M. Wilson, S. Voigt, M. Schulz, A. Wold-
645 Rossby, W.-C. Dullo, A. B. Ronov, A. N. Balukhovsky, and E. Söding (1999),
646 Alternative global Cretaceous paleogeography, in Evolution of the
647 Cretaceous Ocean-Climate System, Geol. Soc. Am. Special Paper 332,
648 edited by E. Barrera and C. C. Johnson, 1-47, Boulder, Colorado.
649 Herbert, T.D. (1992), Paleomagnetic calibration of Milankovitch cyclicity in
650 Lower Cretaceous sediments. Earth. Planet. Sci. Lett,. 112, 15–28.
651 Herbert, T. D. (1997), A long marine history of carbon cycle modulation by
652 orbital-climatic changes. Proceedings of the National Academy of Sciences
653 of the United States of America, 94(16), 8362–8369. doi:
654 10.1073/pnas.94.16.8362
655 Huybers, P. J. (2006), Early Pleistocene glacial cycles and the integrated summer
656 insolation forcing, Science, 313, 508–511, doi:10.1126/ science.1125249.
657 Jones, C.E., and Jenkyns, H.C. (2001), Seawater strontium isotopes, Oceanic
658 Anoxic Events, and seafloor hydrothermal activity in the Jurassic and
659 Cretaceous. American Journal of Science, 301, 112–149.
660 Joo, Y. J., and B. B. Sageman (2014), Cenomanian to Campanian carbon isotope
661 chemostratigraphy from the Western Interior Basin, U.S.A., J. Sediment.
662 Res., 84, 529-542, doi:10.2110/jsr.2014.38.
663 Jarvis, I., A. S. Gale, H. C. Jenkyns, and M. A. Pearce (2006), Secular variation in
664 Late Cretaceous carbon isotopes and sea-level change: evidence from a

new d13C carbonate reference curve for the Cenomanian – Campanian (99.6 – 70.6 Ma), Geol. Mag., 143, 561–608.

Jarvis, I., J. Trabucho-Alexandre, D. R. Gröcke, D. Uličný, and J. Laurin (2015), Intercontinental correlation of organic carbon and carbonate stable isotope records: evidence of climate and sea-level change during the Turonian (Cretaceous), The Depositional Record, 1, 53-90, doi:10.1002/dep2.6.

Kodama, K. P., and Hinnov, L. A. (2014), Rock magnetic cyclostratigraphy. Oxford, UK: Wiley-Blackwell. https://doi.org/10.1002/9781118561294

Košťák, M., Čech, S., Uličný, D., Sklenář, J., Ekrt, B., and Mazuch, M. (2018), Ammonites, inoceramids and stable carbon isotopes of the CenomanianeTuronian OAE2 interval in central Europe: Pecínov quarry, Bohemian Cretaceous Basin (Czech Republic). Cretaceous Research, 87, 150-173.

Kump, L. R., and M. A. Arthur (1999), Interpreting carbon–isotope excursions: Carbonate and organic matter, Chem. Geol., 161, 181–198, doi:10.1016/S0009-2541(99)00086-8.

Laskar, J., P. Robutel, F. Joutel, M. Gastineau, A.C.M. Correia, and B. Levrard (2004), A long-term numerical solution for the insolation quantities of the Earth, Astron. Astrophys., 428, 261–285, doi:10.1051/0004-6361:20041335.

Laskar, J., Fienga, A., Gastineau, M., and Manche, H. (2011a), La2010: A new orbital solution for the long term motion of the Earth: Astronomy and Astrophysics, 532, A89, doi:10.1051/0004-6361/201116836.

689 Laskar, J., Gastineau, M., Delisle, J-B., Farrés, A., and Fienga, A. (2011b), Strong
690 chaos induced by close encounters with Ceres and Vesta: Astronomy and
691 Astrophysics, 532, L4, doi: 10.1051/0004-6361/201117504.
692 Laurin, J., Meyers, S.R., Galeotti, S., and Lanci, L. (2016), Frequency modulation
693 reveals the phasing of orbital eccentricity during Cretaceous Oceanic
694 Anoxic Event II and the Eocene hyperthermals. Earth and Planetary
695 Science Letters, 442, 143-156, doi:10.1016/j.epsl.2016.02.047.
696 Laurin, J., S. R. Meyers, D. Uličný, I. Jarvis, and B. B. Sageman (2015), Axial
697 obliquity control on the greenhouse carbon budget through middle- to
698 high-latitude reservoirs, Paleoceanography, 30, 133-149,
699 doi:10.1002/2014PA002736
700 Laurin, J., Růžek, B., and Giorgioni, M. (2017), Orbital signals in carbon isotopes:
701 phase distortion as a signature of the carbon cycle. Paleoceanography, 32,
702 1236–1255. doi: 10.1002/2017PA003143
703 Liu, H.S. (1998), Glacial-interglacial changes induced by pulse modulation of the
704 incoming solar radiation. J. Geophys. Res. 103(D20), 26147–26164.
705 Ma, C., S. R. Meyers, B. B. Sageman, B. S. Singer, and B. R. Jicha (2014), Testing the
706 astronomical time scale for oceanic anoxic event 2, and its extension into
707 Cenomanian strata of the Western Interior Basin (USA), Geol. Soc. Am.
708 Bul., 126, 974-989.
709 Ma, C., Meyers, S.R., and Sageman, B.B. (2019), Testing Late Cretaceous
710 astronomical solutions in a 15 million year astrochronologic record from
711 North America. Earth and Planetary Science Letters, 513, 1-11.
712 Malinverno, A., E. Erba, and T. Herbert (2010), Orbital tuning as an inverse
713 problem: Chronology of the early Aptian oceanic anoxic event 1a (Selli

714 Level) in the Cismon APTICORE, Paleoceanography, 25, PA2203,
715 doi:10.1029/2009PA001769.
716 Marple, S. L. (1999), Computing the discrete-time analytic signal via FFT. IEEE
717 Transactions on Signal Processing, 47(9), 2600–2603,
718 doi:10.1109/78.782222.
719 Meyers, S. R. (2014), astrochron: An R Package for Astrochronology (Version
720 0.3.1). http://www.geology.wisc.edu/~smeyers.
721 Meyers, S.R. (2015), The evaluation of eccentricity-related amplitude modulation
722 and bundling in paleoclimate data: An inverse approach for
723 astrochronologic testing and time scale optimization: Paleoceanography,
724 30, doi:10.1002/2015PA002850.
725 Meyers, S. R., S. E. Siewert, B. S. Singer, B. B. Sageman, D. J. Condon, J. D.
726 Obradovich, B. R. Jicha, and D. A. Sawyer (2012a), Intercalibration of
727 radioisotopic and astrochronologic time scales for the Cenomanian-
728 Turonian boundary interval, Western Interior Basin, USA, Geology, 40, 7-
729 10, doi:10.1130/G32261.1.
730 Meyers, S. R., B. B. Sageman, and M. A. Arthur (2012b), Obliquity forcing of
731 organic matter accumulation during Oceanic Anoxic Event 2,
732 Paleoceanography, 27, PA3212, doi:10.1029/2012PA002286.
733 Meyers, S.R., Sageman, B.B., and Hinnov, L.A. (2001), Integrated quantitative
734 stratigraphy of the Cenomanian-Turonian Bridge Creek Limestone
735 Member using evolutive harmonic analysis and stratigraphic modeling:
736 Journal of Sedimentary Research, 71, 628-644.

737 Meyers, S.R., and Sageman, B.B. (2007), Quantification of deep-time orbital
738 forcing by average spectral misfit: American Journal of Science, 307, 773–
739 792, doi:10.2475/05.2007.01.
740 Pearce, M.A., Jarvis, I., Ball, P.J., and Laurin, J. (2020), Palynology of the
741 Cenomanian to lowermost Campanian (Upper Cretaceous) Chalk of the
742 Trunch Borehole (Norfolk, UK) and a new dinoflagellate cyst bioevent
743 stratigraphy for NW Europe. Review of Palaeobotany and Palynology, 278,
744 104188, doi:10.1016/j.revpalbo.2020.104188.
745 Pucéat, E., C. Lecuyer, S. M. F. Sheppard, G. Dromart, S. Reboulet, and P. Grandjean
746 (2003), Thermal evolution of Cretaceous Tethyan marine waters inferred
747 from oxygen isotope composition of fish tooth enamels,
748 Paleoceanography, 18 (2), 1029, doi:10.1029/2002PA000823.
749 Raymo, M. E., and K. Nisancioglu (2003), The 41 kyr world: Milankovitch's other
750 unsolved mystery, Paleoceanography, 18(1), 1011,
751 doi:10.1029/2002PA000791.
752 R Core Team (2015), R: A language and environment for statistical computing. R
753 Foundation for Statistical Computing, Vienna, Austria. http://www.R-
754 project.org/.
755 Rossignol-Strick, M. (1983), African monsoons, an immediate climate response
756 to orbital insolation. Nature 304, 46–49.
757 Sageman, B. B., S. R. Meyers, and M. A. Arthur (2006), Orbital time scale and new
758 C-isotope record for Cenomanian-Turonian boundary stratotype, Geology,
759 34, 125-125.
760 Schlanger, S., Jenkyns, H. (1976). Cretaceous oceanic anoxic events: causes and
761 consequences. Geol. Mijnb. 55, 179–184.

762 Short, D. A., J. G. Mengel, T. J. Crowley, W. T. Hyde, and G. R. North (1991),
763 Filtering of Milankovitch cycles by Earth's geography, Quat. Res., 35, 157–
764 173, doi:10.1016/0033-5894(91)90064-C.
765 Sprovieri, M., N. Sabatino, N. Pelosi, S. J. Batenburg, R. Coccioni, M. Iavarone, and
766 S. Mazzola (2013), Late Cretaceous orbitally-paced carbon isotope
767 stratigraphy from the Bottaccione Gorge (Italy), Palaeogeogr.,
768 Palaeoclimatol. Palaeoecol., 379–380, 1–94,
769 doi:10.1016/j.palaeo.2013.04.006.
770 Stoll, H. and Schrag, D. (2000), High-resolution stable isotope records from the
771 Upper Cretaceous rocks of Italy and Spain: Glacial episodes in a
772 greenhouse planet? Geol. Soc. Am. Bull., 112, 308–319.
773 Taner, M. T. (1992), Attributes revisited, technical publication. Rock solid images,
774 Inc., Houston, TX. Retrieved from http://rocksolidimages.
775 com/pdf/attrib_revisited.htm (updated 2003).
776 Thomson, D.J. (1982), Spectrum estimation and harmonic analysis: Proc. IEEE, v.
777 70, p. 1055–1096.
778 Uličný, D., Laurin, J., and Čech, S. (2009), Controls on clastic sequence geometries
779 in a shallow- marine, transtensional basin: the Bohemian Cretaceous
780 Basin, Czech Republic: Sedimentology, 56, 1077–1114.
781 Uličný, D., Jarvis, I., Gröcke, D.R., Čech, S., Laurin, J., Olde, K., Trabucho-Alexandre,
782 J., Švábenická, L. and Pedenychouk, N. (2014), A high-resolution carbon-
783 isotope record of the Turonian stage correlated to a siliciclastic basin fill:
784 Implications for mid-Cretaceous sea-level change: Palaeogeography
785 Palaeoclimatology Palaeoecology, 405, 42–58.

786 Voigt, S., J. Erbacher, J. Mutterlose, W. Weiss, T. Westerhold, F. Wiese, M. Wilmsen,
787 T. Wonik (2008), The Cenomanian–Turonian of the Wunstorf section
788 (North Germany): global stratigraphic reference section and new orbital
789 time scale for Oceanic Anoxic Event 2, Newslett. Stratigr., 43, 65–89.
790 Voigt, S., Aurag, A., Leis, F. and Kaplan, U. (2007), Late Cenomanian to Middle
791 Turonian high-resolution carbon isotope stratigraphy: new data from the
792 Mu!nsterland Cretaceous Basin, Germany. Earth Planet. Sci. Lett., 253, 196.
793 Waltham, D. (2015), Milankovitch period uncertainties and their impact on
794 cyclostratigraphy, J. Sediment. Res., 85, 990-998, doi:10.2110/jsr.2015.66
795 Wendler, I. (2013), A critical evaluation of carbon isotope stratigraphy and
796 biostratigraphic implications for Late Cretaceous global correlation, Earth
797 Sci. Rev., 126, 116-146, doi:10.1016/j.earscirev.2013.08.003.
798 Wendler, J. E., S. R. Meyers, I. Wendler, and J. Kuss (2014), A million-year-scale
799 astronomical control on Late Cretaceous sea-level. Newsl. Stratigr., 47, 1-
800 19, doi:10.1127/0078-0421/2014/0038.
801 Wu, H., Zhang, S., Jiang, G., Hinnov, L., Yang, T., Li, H., Wan, X., Wang, C. (2013),
802 Astrochronology of the Early Turonian–Early Campanian terrestrial
803 succession in the Songliao Basin, northeastern China and its implications
804 for long-period behavior of the Solar System. Palaeogeogr. Palaeoclimatol.
805 Palaeoecol., 385, 55–70.
806 Zeebe, R.E. (2017), Numerical Solutions for the Orbital Motion of the Solar
807 System over the Past 100 Myr: Limits and New Results, The Astronomical
808 Journal, 154, no. 5, doi: 10.3847/1538-3881/aa8cce

809 Zeebe, R.E., and Lourens, L.J. (2019), Solar System chaos and the Paleocene–
810 Eocene boundary age constrained by geology and astronomy. Science,
811 365 (6456), 926-929, doi:10.1126/science.aax0612.
812 Zeebe, R. E., Westerhold, T., Littler, K., & Zachos, J. C. (2017), Orbital forcing of the
813 Paleocene and Eocene carbon cycle. Paleoceanography, 32, 440–465.
814 https://doi.org/10.1002/2016PA003054
815 Zeeden, C., Meyers, S.R., Lourens, L.J., Hilgen, F.J. (2015), Testing astronomically
816 tuned age models, Paleoceanography, 30, 369-383, doi:
817 10.1002/2014PA002762.

FIGURE CAPTIONS

Table 1. Comparison of published age estimates for the Early Turonian. CIE = carbon-isotope excursion; n.d. = not defined explicitly.

Table 2. Age calibration of chronostratigraphic boundaries and carbon-isotope excursions (CIE) in reference boreholes. C.w. = *Collignoniceras woollgari*. CI = confidence interval.

Figure 1. Overview of chronology (GTS2012; Gradstein et al. 2012) and carbon-isotope stratigraphy of the study interval. Major carbon-isotope anomalies (CIEs) are highlighted by blue shading (positive anomalies) and yellow shading (negative anomalies). The Lower/Middle Turonian boundary is defined by the first occurrence (FO) of *Collignoniceras woollgari*, which is penecontemporaneous with the Lulworth CIE (Jarvis et al. 2006). **(a)** English Chalk reference curve; modified after Jarvis et al. (2006); age calibration after Pearce et al. (2020). **(b)** Borehole Bch-1, Bohemian Cretaceous Basin (Uličný et al. 2014; Jarvis et al. 2015). **(c)** USGS #1 Portland core, Western Interior Basin; lower part (black) after Sageman et al. 2006 ("min option" in their fig. 1); upper part (blue) after Joo and Sageman (2014). **(d)** Wunstorf core, age calibrated (floating astrochronology after Voigt et al. 2008). **(e)** Contessa section plotted in the depth domain (Stoll and Schrag 2000). **(f)** Eccentricity maxima interpreted by Batenburg et al. (2016).

842 **Figure 2.** Paleogeographic context. **(a)** Plate tectonic reconstruction after Hay et
843 al. (1999). Land/sea distribution is simplified after the PALEOMAP Project, C.R.
844 Scotese (www.scotese.com). BCB = the Bohemian Cretaceous Basin. **(b)** Detail of
845 the study area (modified after Uličný et al. 2009, 2014) plotted in the present-
846 day coordinate system.
847
848 **Figure 3.** Reference boreholes and data discussed in this study. Numbers 1a
849 through 46 denote correlation markers (see Figs. S1-S6 for a detailed correlation
850 and Figs. S7-S8 for lithology). Carbon isotope excursions in the Lower Turonian
851 are labelled "se-20", "be-20", etc., where "se" and "be" refer to the location
852 (Sedlec and Beřkovice, respectively). Grey shading highlights the Oceanic Anoxic
853 Event II (OAE II). GR = gamma ray, RES = resistivity, XNN = neutron-neutron log.
854 Blue shading marks the correlation uncertainty of the Cenomanian-Turonian and
855 Lower-Middle Turonian boundaries (Figs. S1-S6 and S13). Type A cycles =
856 carbonate-dominated lithofacies; Type B = siliciclastic-dominated lithofacies
857 (Figs. S7 and S8). Lithostratigraphy after Čech et al. (1980). Genetic sequences
858 after Uličný et al. (2009). Wavy line = omission surface.
859
860 **Figure 4**. Spectral estimates, borehole J-719670. **(a)** Resistivity log (RES). Labels
861 1a through 45 denote correlation markers most of which correspond to maxima
862 in the S_4 signal. **(b)** MTM (3 2π) amplitude estimate for the common logarithm of
863 RES obtained with a 7-m moving window (EHA). F-test significance estimates are
864 presented in Fig. S9. Potential signals are labelled S_1 through S_4. Interference
865 patterns (IP) are highlighted by arches ")". Note that the amplitude and F-test
866 maxima corresponding to the S_4 signal migrate towards lower frequencies

867 paralleling an upward increase in sand contents and a large-scale progradational
868 pattern in the coeval siliciclastic system (Fig. S1). The EHA pattern resembles a
869 reciprocal function of signal wavelength, consistent with a linear increase in
870 sedimentation rate. **(c)** Resistivity log and EHA amplitude after removal of the
871 linear trend. Intervals of constructive interference of S_{4a} and S_{4b} signals (x)
872 delineate ~100-kyr eccentricity maxima. **(d)** MTM and ASM results for the
873 interval 380-418m. The ASM analysis is based on all F-test maxima exceeding the
874 0.90 level between frequencies 0 and 5 cycle/m. Ho/SL = null-hypothesis
875 significance level. Sedimentation rates constrained by GTS2012 are shown by
876 ochre shading. Blue lines and symbols indicate the best fit to the astronomical
877 terms of long eccentricity (E_1; 405 kyr period), short eccentricity ($E_{2,3}$; 127 and
878 97 kyr periods), obliquity ($O_{1,2}$; 49 and 39 kyr periods) and precession (P_{1-4}; 23 -
879 19 kyr periods; Tab. S2a).
880
881 **Figure 5**. Correlation of astronomical signals. **(a, b)** Astronomical signatures in
882 boreholes J-719670 and J-650704; setup as in Fig. 4. Intervals of constructive
883 interference of the S_{4a} and S_{4b} signals (x) delineate ~100-kyr eccentricity
884 maxima. Series of strong interference patterns (IP) in the EHA plot mark 405-kyr
885 maxima (ochre shading) superimposed upon a maximum in ~2.4-Myr
886 modulation (cf. Fig. 5c). Note that the fidelity of S_4 envelopes and polarity of S_1
887 (405-kyr) signals would remain uncertain without IP (cf. Laurin et al. 2016). **(c)**
888 Comparison with the astronomical solution La2010d (Laskar et al. 2011a); the
889 nearest interval compatible with eccentricity phasing in the study interval. Filter
890 setup (Taner, roll-off rate 4×10^4): J-719670, S_4 = 1.00±0.30 cycle/m, S_2 =
891 0.20±0.05 cycle/m, S_1 = 0.05±0.01 cycle/m; J-650704, S_4 = 1.15±0.35 cycle/m, S_2

892 = 0.23±0.05 cycle/m, S_1 = 0.05±0.01 cycle/m; La2010d, prec. = 50±15 cycle/Myr,
893 short ecc. = 10±3 cycle/Myr, long ecc. = 2.47±0.5 cycle/Myr.
894
895 **Figure 6.** Interpretation of astronomical signatures, borehole 4523-A. **(a)**
896 Carbon-isotope data, greyscale and filtered signals. Filter setup (Taner, roll-off
897 rate 4×10^4): S_4 = 1.00±0.30 cycle/m, S_2 = 0.23±0.05 cycle/m. **(b)** EHA spectral
898 estimate for greyscale data; dashed lines denote the expected trace of the S_4
899 (precessional) signal inferred from correlation to borehole J-719670 (5-m
900 moving average). **(c)** MTM and ASM estimates for greyscale data, interval 190-
901 203 m. See Tables S2a and S2b for ASM setup. Sedimentation rates constrained
902 by GTS2012 are shown by ochre shading.
903
904 **Figure 7.** Eccentricity framework constraining the tuning target (see also Figs.
905 S14 and S15). **(a-d)** Filtered precessional and eccentricity signals in reference
906 boreholes. Maxima in short-eccentricity cycles (~100 kyr; labelled ecc1 through
907 ecc11) are inferred using a combination of bandpassed S_2 and amplitude
908 envelopes of the precessional signal (S_4): in the middle and upper parts of the
909 succession that exhibit distinct precessional modulations (Fig. 5), the ~100-kyr
910 maxima are based primarily on amplitude envelopes of the S_4 signal in borehole
911 J-719670; the lower part of the succession exhibits less stable precessional
912 signals; ~100-kyr maxima ecc1-ecc3 are therefore placed at maxima in the S_2
913 bandpass (see text). Long-eccentricity, 405-kyr, maxima (ochre shading) are
914 placed at intervals with strong precessional interference patterns (Figs. 4 and 5).
915 **(e)** Bundling ratios of precessional (P) vs. short-eccentricity (E) signals in the
916 study interval. **(f)** Correlation to the nearest compatible segments of the

917 astronomical solutions La2010d (Laskar et al. 2011a) and La2004 (Laskar et al.
918 2004). Filter setup (Taner, roll-off rate 4×10^4): Bch-1, S_2 = 0.15±0.04 cycle/m;
919 4523-A, S_4 = 1.00±0.30 cycle/m, S_2 = 0.23±0.05 cycle/m, S_1 = 0.05±0.01 cycle/m;
920 J-719670, S_4 = 1.00±0.30 cycle/m, S_2 = 0.20±0.05 cycle/m, S_1 = 0.05±0.01
921 cycle/m; J-650704, S_4 = 1.15±0.35 cycle/m, S_2 = 0.23±0.05 cycle/m, S_1 =
922 0.05±0.01 cycle/m; La2004 and La2010d, prec. = 50±15 cycle/Myr, short ecc. =
923 10±3 cycle/Myr, long ecc. = 2.47±0.5 cycle/Myr.
924
925 **Figure 8.** Updated chronology and eccentricity phasing for the Early Turonian.
926 **(a)** Chronology; duration of the Early Turonian is estimated as 885 ±46 kyr (Tab.
927 2); the floating astrochronology is anchored to the GTS2012 age of the C/T
928 bondary (93.9 ±0.15 Myr ago). Duration of the Cenomanian part of OAE II
929 (shaded) is based on Sageman et al. (2006) and Ma et al. (2014); Fig. S13. **(b)** The
930 nearest segment of the astronomical solution La2010d (Laskar et al. 2011a)
931 whose eccentricity phasing is compatible with eccentricity signatures in the
932 study interval (Figs. 4, 5 and 7). Filter setup as in Figure 7. Well-preserved
933 modulation in the middle and upper parts of the study interval suggests that
934 these intervals overlap with a ~2.4-Myr eccentricity maximum. If so, then OAE II
935 coincides with a node in the 2.4-Myr cycle, in agreement with previous results
936 (Batenburg et al. 2016; Laurin et al. 2016). **(c)** Timing of 405-kyr eccentricity
937 maxima (ochre shading) and minima inferred in this study. Comparison with
938 eccentricity phasing at Furlo (Italy) is shown at the bottom; IRM = Isothermal
939 Remanent Magnetization; black = sum of eccentricity components; red = 405 kyr
940 (Laurin et al. 2016). **(d)** EHA estimate for age-calibrated $\delta^{13}C_{org}$, borehole 4523-A.
941 **(e)** Age-calibrated carbon-isotope curves. The Early Turonian interval of 4523-A

942 is calibrated in high-resolution as described in sections 4.4 and 4.5. A linear
943 sedimentation rate of 1.55 cm/kyr is applied to the Cenomanian segment of
944 4523-A, beneath marker 1a (grey part of $\delta^{13}C$ curve; Fig. S13). Local isotope
945 excursions are indicated ("se-6", etc.). Age calibration of the Wunstorf record is
946 adopted from Voigt et al. (2008). English Chalk (Jarvis et al. 2006; Pearce et al.
947 2020) and Portland (black: Sageman et al. 2006; blue: Joo and Sageman 2014)
948 records are recalibrated in the time domain by linearly adjusting the duration of
949 the Early Turonian. Abbreviations: *I.c.* = *Inoceramus cuvieri, C.w.* = *Collignoniceras*
950 *woollgari, M.n.* = *Mammites nodosoides, M.pu.* = *Mytiloides puebloensis, W.d.* =
951 *Watinoceras devonense, M.g.* = *Metoicoceras geslinianum.*

Reference	Location	Duration of Early Turonian [Myr]	Un-certainty [± Myr]	Pros	Cons
Sageman et al. (2006); Meyers et al. (2012a)	Portland	0.785	n.d.	Robust astronomical signature	Short-eccentricity tuning target, monochromatic (95 kyr); modulation of the tuning target not considered
Voigt et al. (2008)	Wunstorf	0.84	n.d.	Precession-scale resolution; robust astronomical signature	Precession-paced chronology does not reach the top of Early Turonian; modulation of the tuning target not considered
Gradstein et al. 2012 (GTS 2012)		1.0	n.d.		Meyers et al. (2012a) misquoted [1]); Voigt et al. (2008) not considered
Sprovieri et al. (2013)	Bottaccione	0.6-0.8	n.d.	Well-defined 405-kyr signature	No ammonite zonation; reduced resolution near C/T boundary
Eldrett et al. (2015; their fig. 11)	Iona	1.14	n.d.	High-resolution astronomical signature	No ammonite zonation; Early/Middle Turonian boundary placed deep into a major positive CIE (runup to Round Down CIE)
Batenburg et al. (2016)	Contessa	0.6-1.2	n.d.	Well-defined eccentricity signature	No ammonite zonation; C/T boundary controversial (cf. Wendler 2013; Fig. 1)
This study	Bohemian Cretaceous Basin	0.885	0.046	Precession-scale resolution; robust eccentricity phasing; modulation of the tuning target included in uncertainty	Biostratigraphy correlated from adjacent boreholes (correlation uncertainty acknowledged in the uncertainty range)

[1]) The duration of W. devonense Zone is given as 0.35 Myr with reference to Meyers et al. (2012a); Meyers et al. (2012a), however, indicate ~0.2 Myr (two short-eccentricity cycles; their figure 1).

Table 1. Comparison of published age estimates for the Early Turonian. CIE = carbon-isotope excursion; n.d. = not defined explicitly.

Stratigraphic level		J-719670			J-650704			4523-A	
	depth [m]	mean floating age [kyr]	uncert. 95% CI [kyr]	depth [m]	mean floating age [kyr]	uncert. 95% CI [kyr]	depth [m]	mean floating age [kyr]	uncert. 95% CI [kyr]
base Middle Turonian (FO *C.w.*), upper limit	360.7	902	+20/-16	384.9	903	+14/-14	144.50	915	+22/-29
Lulworth CIE (δ^{13}C trough)							146.75	890	+27/-22
base Middle Turonian (FO *C.w.*), lower limit	364.5	865	+19/-22	391.0	860	+19/-22	148.50	872	+21/-23
CIE "se-20" peak							178.75	521	+21/-19
CIE "se-10" peak							185.75	315	+20/-18
CIE "se-6" peak							191.25	203	+15/-12
CIE "se-e2o" peak							196.25	79	+16/-15
C/T boundary, upper limit	423.6	11	+17/-7	446.8	11	+22/-7	198.75	17	+16/-9
C/T boundary, lower limit	424.5	-13	+3/-4	447.5	-15	+3/-3	199.75	-9	+3/-2
Onset of OAE II recovery							199.75	-9	+3/-2
Duration of Early Turonian		**885**	**±46 [1])**		884	±49 [1])		890	±53 [1])

[1]) Combined uncertainty, calculated using summation in quadrature
C.w. = *Collignoniceras woollgari*
CI = confidence interval

Table 2. Age calibration of chronostratigraphic boundaries and carbon-isotope excursions (CIE) in reference boreholes.

Figure 1.

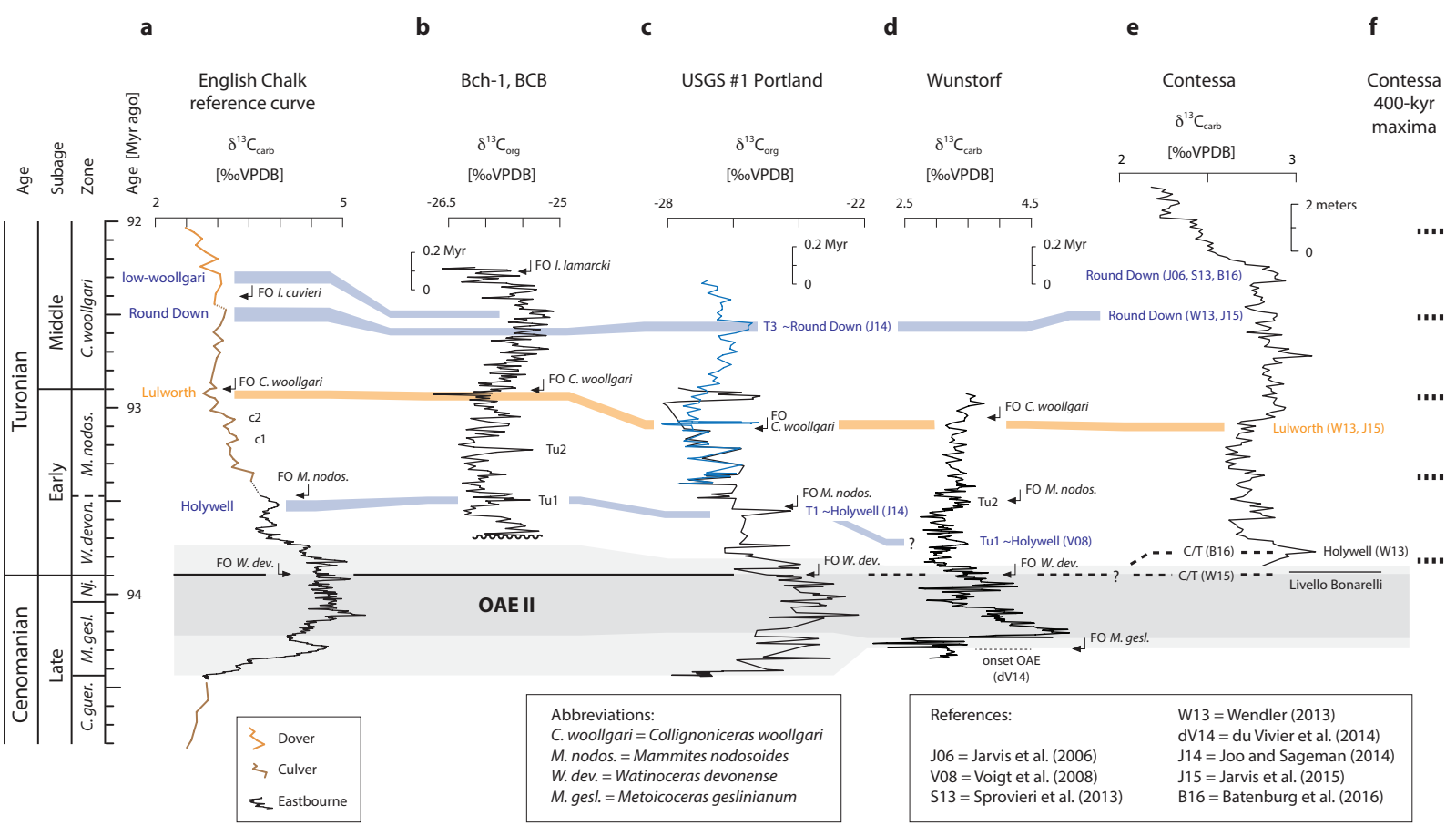
a
b
c
d
e
f
English Chalk reference curve
Bch-1, BCB
USGS #1 Portland
Wunstorf
Contessa
Contessa 400-kyr maxima
Age
Subage
Zone
Age [Myr ago]
δ13Ccarb [‰VPDB]
δ13Corg [‰VPDB]
2
5
-26.5
-25
-28
-22
2.5
4.5
3
92
93
94
Turonian
Cenomanian
Middle
Early
Late
C. woollgari
M. nodos.
W. devon.
Nj.
M. gesl.
C. guer.
low-woollgari
Round Down
Lulworth
Holywell
FO I. cuvieri
FO I. lamarcki
FO C. woollgari
FO M. nodos.
FO W. dev.
FO M. gesl.
c2
c1
Tu2
Tu1
T3 ~Round Down (J14)
T1 ~Holywell (J14)
Tu1 ~Holywell (V08)
Round Down (J06, S13, B16)
Round Down (W13, J15)
Lulworth (W13, J15)
Holywell (W13)
C/T (B16)
C/T (W15)
Livello Bonarelli
0.2 Myr
0
2 meters
OAE II
onset OAE (dV14)
Dover
Culver
Eastbourne
Abbreviations:
C. woollgari = Collignoniceras woollgari
M. nodos. = Mammites nodosoides
W. dev. = Watinoceras devonense
M. gesl. = Metoicoceras geslinianum
References:
J06 = Jarvis et al. (2006)
V08 = Voigt et al. (2008)
S13 = Sprovieri et al. (2013)
W13 = Wendler (2013)
dV14 = du Vivier et al. (2014)
J14 = Joo and Sageman (2014)
J15 = Jarvis et al. (2015)
B16 = Batenburg et al. (2016)

Figure 2.

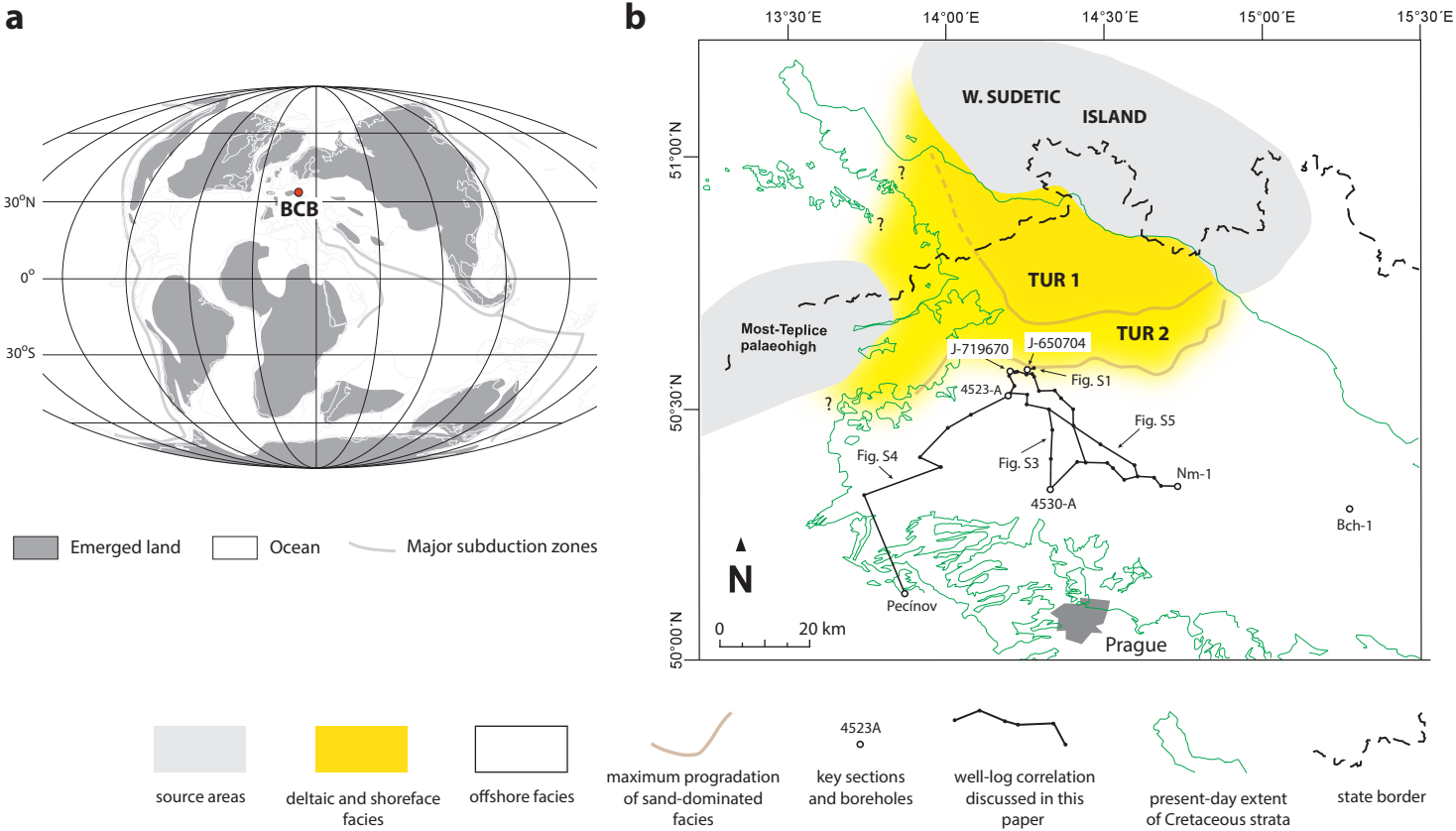
a
30°N
0°
30°S
BCB
Emerged land
Ocean
Major subduction zones
b
13°30´E
14°00´E
14°30´E
15°00´E
15°30´E
51°00´N
50°30´N
50°00´N
W. SUDETIC
ISLAND
TUR 1
TUR 2
Most-Teplice
palaeohigh
J-719670
J-650704
Fig. S1
4523-A
Fig. S5
Fig. S4
Fig. S3
Nm-1
4530-A
Bch-1
N
0
20 km
Pecínov
Prague
source areas
deltaic and shoreface facies
offshore facies
maximum progradation of sand-dominated facies
4523A
key sections and boreholes
well-log correlation discussed in this paper
present-day extent of Cretaceous strata
state border

Figure 3.

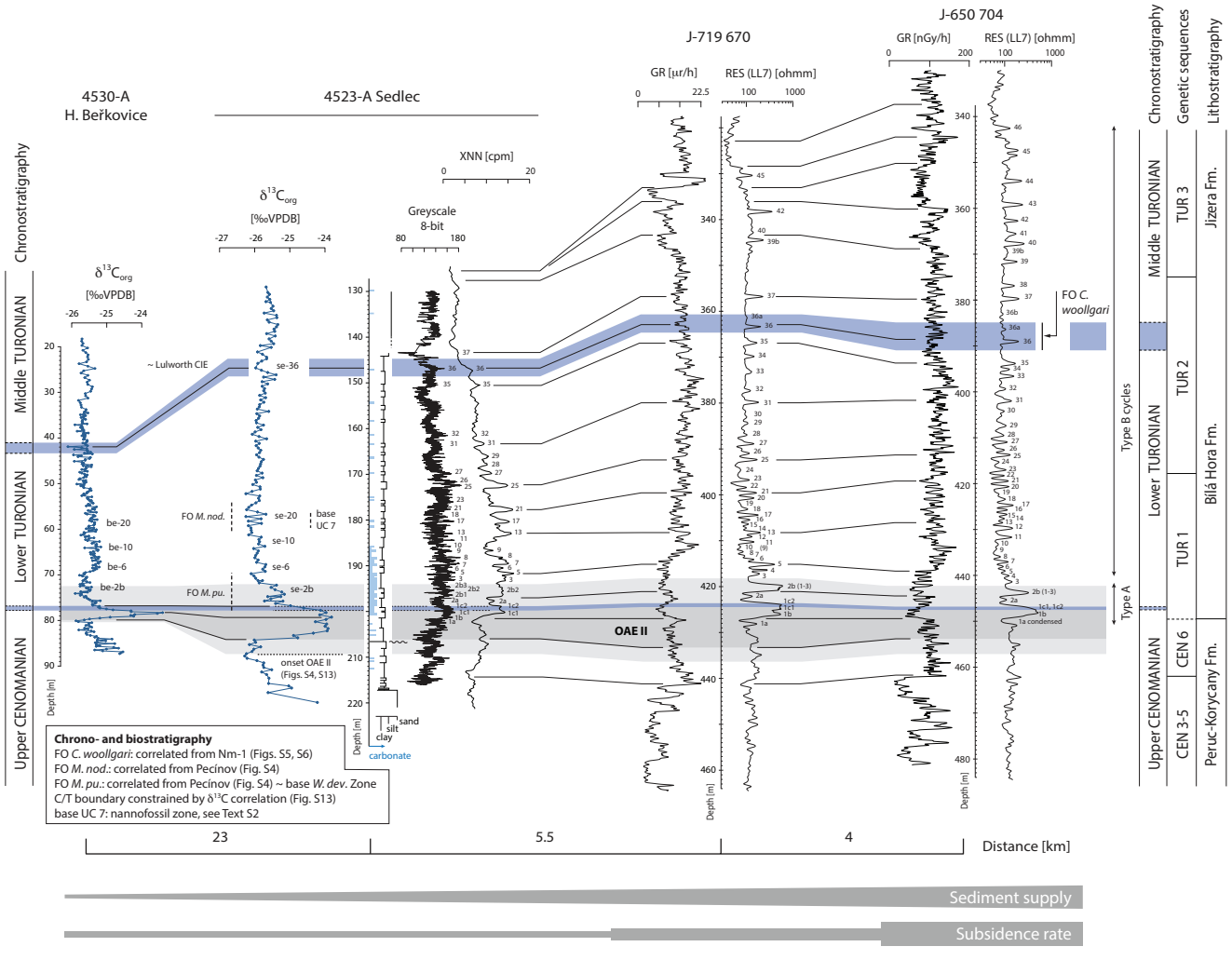
4530-A
H. Beřkovice
4523-A Sedlec
J-719 670
J-650 704
GR [µr/h]
RES (LL7) [ohmm]
GR [nGy/h]
RES (LL7) [ohmm]
XNN [cpm]
Greyscale 8-bit
δ13Corg [‰VPDB]
~ Lulworth CIE
FO M. nod.
FO M. pu.
base UC 7
onset OAE II (Figs. S4, S13)
OAE II
FO C. woollgari
Type B cycles
Type A
sand
silt
clay
carbonate
Depth [m]
Distance [km]
23
5.5
4
Chronostratigraphy
Genetic sequences
Lithostratigraphy
Middle TURONIAN
Lower TURONIAN
Upper CENOMANIAN
TUR 3
TUR 2
TUR 1
CEN 6
CEN 3-5
Jizera Fm.
Bílá Hora Fm.
Peruc-Korycany Fm.
Chrono- and biostratigraphy
FO C. woollgari: correlated from Nm-1 (Figs. S5, S6)
FO M. nod.: correlated from Pecínov (Fig. S4)
FO M. pu.: correlated from Pecínov (Fig. S4) ~ base W. dev. Zone
C/T boundary constrained by δ13C correlation (Fig. S13)
base UC 7: nannofossil zone, see Text S2
Sediment supply
Subsidence rate

Figure 4.

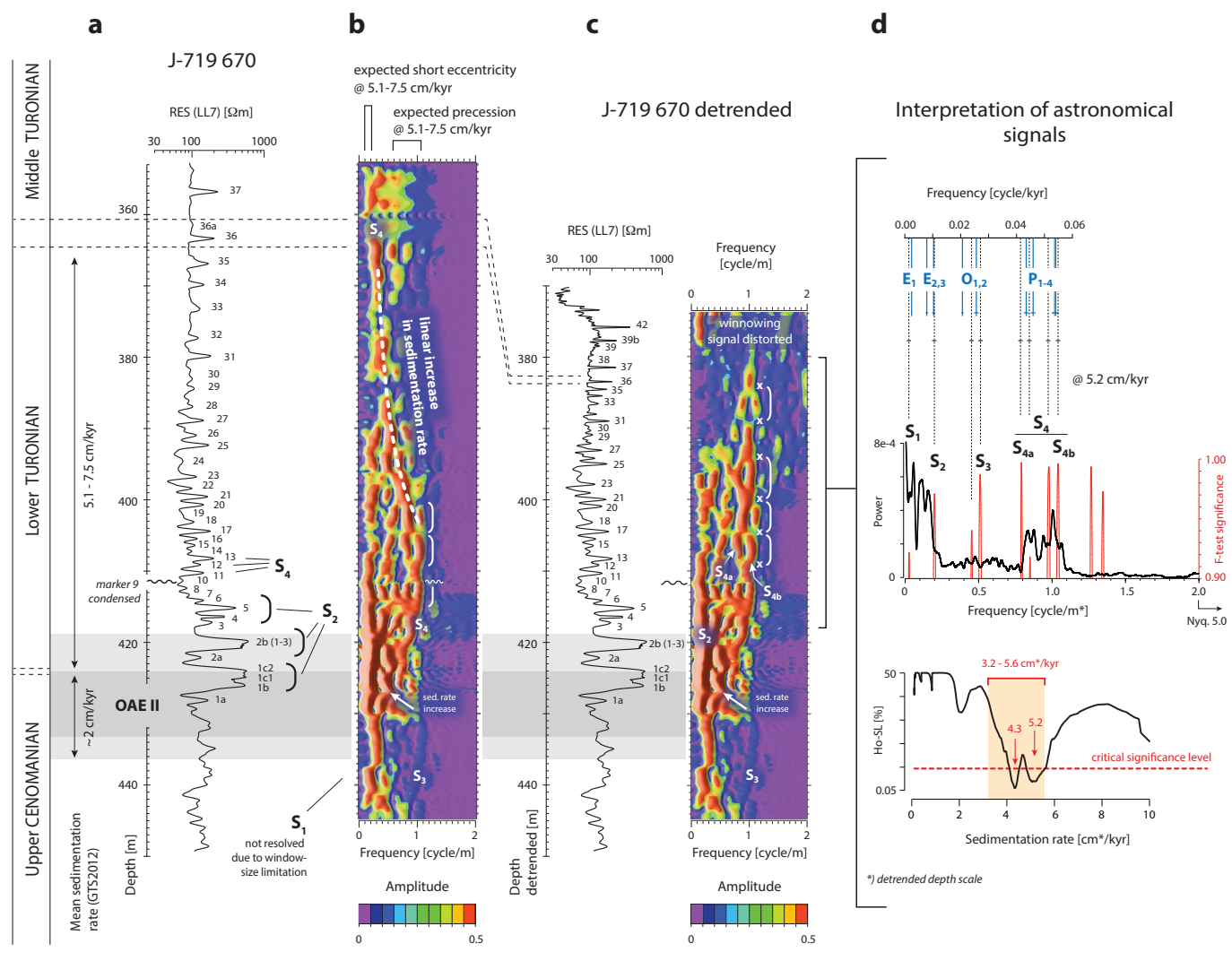
a
J-719 670
RES (LL7) [Ωm]
30
100
1000
Middle TURONIAN
Lower TURONIAN
Upper CENOMANIAN
5.1 - 7.5 cm/kyr
~2 cm/kyr
OAE II
marker 9
condensed
S4
S2
S1
not resolved
due to window-
size limitation
Depth [m]
Mean sedimentation
rate (GTS2012)
b
expected short eccentricity
@ 5.1-7.5 cm/kyr
expected precession
@ 5.1-7.5 cm/kyr
linear increase
in sedimentation rate
sed. rate
increase
S3
Frequency [cycle/m]
Amplitude
c
J-719 670 detrended
RES (LL7) [Ωm]
Frequency
[cycle/m]
winnowing
signal distorted
S4a
S4b
Depth
detrended [m]
d
Interpretation of astronomical
signals
Frequency [cycle/kyr]
E1
E2,3
O1,2
P1-4
@ 5.2 cm/kyr
Power
F-test significance
Frequency [cycle/m*]
Nyq. 5.0
3.2 - 5.6 cm*/kyr
Ho-SL [%]
4.3
5.2
critical significance level
Sedimentation rate [cm*/kyr]
*) detrended depth scale

Figure 5.

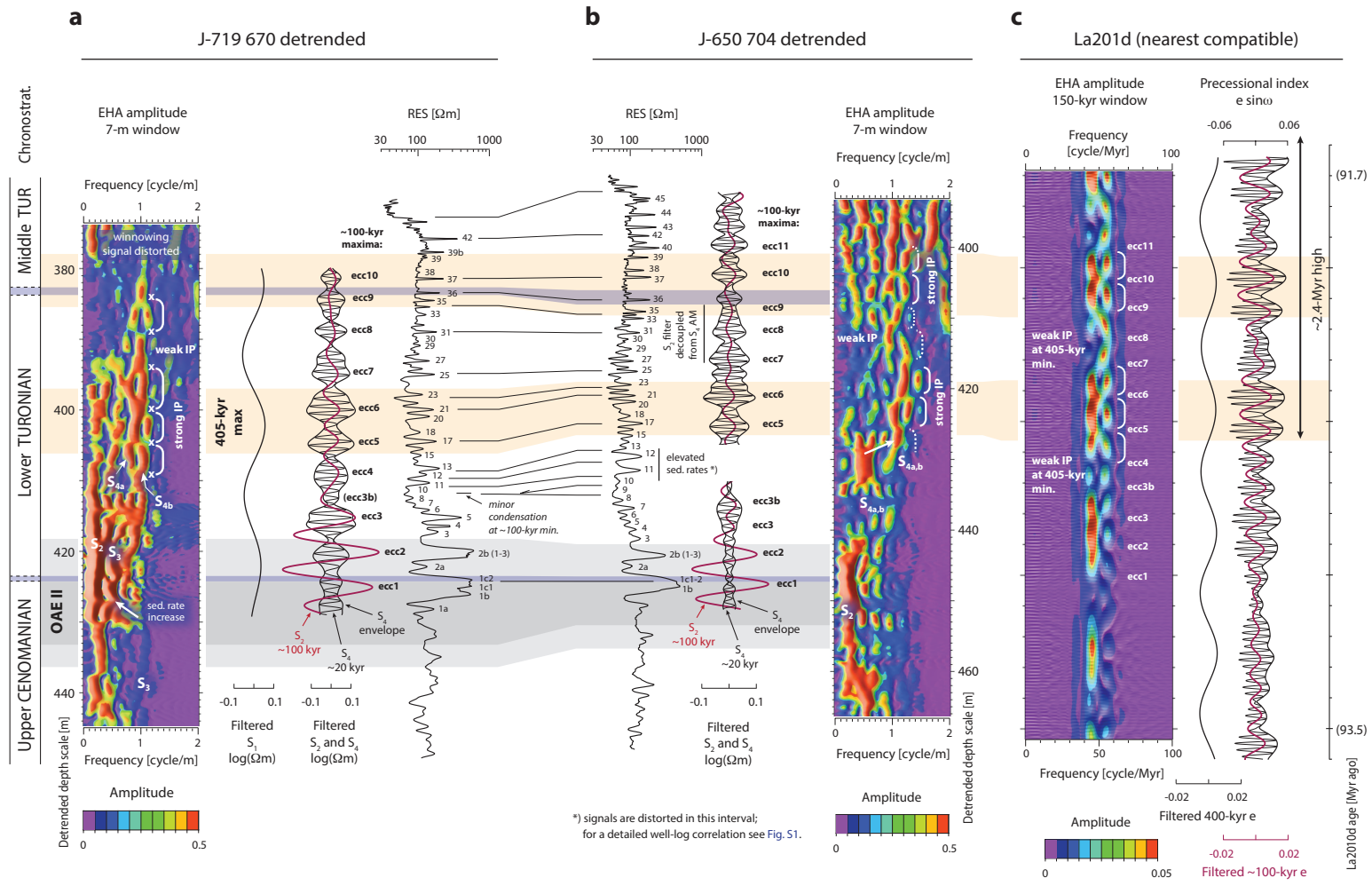
a
J-719 670 detrended
b
J-650 704 detrended
c
La201d (nearest compatible)
Chronostrat.
Middle TUR
Lower TURONIAN
Upper CENOMANIAN
OAE II
EHA amplitude
7-m window
Frequency [cycle/m]
winnowing
signal distorted
weak IP
strong IP
sed. rate
increase
RES [Ωm]
~100-kyr
maxima:
405-kyr
max
minor
condensation
at ~100-kyr min.
elevated
sed. rates *)
S, filter
decoupled
from S4 AM
envelope
~100 kyr
~20 kyr
Filtered
S1
log(Ω m)
Filtered
S2 and S4
log(Ω m)
Detrended depth scale [m]
Amplitude
*) signals are distorted in this interval;
for a detailed well-log correlation see Fig. S1.
EHA amplitude
150-kyr window
Frequency
[cycle/Myr]
Precessional index
e sinω
weak IP
at 405-kyr
min.
~2.4-Myr high
Filtered 400-kyr e
Filtered ~100-kyr e
La2010d age [Myr ago]

Figure 6.

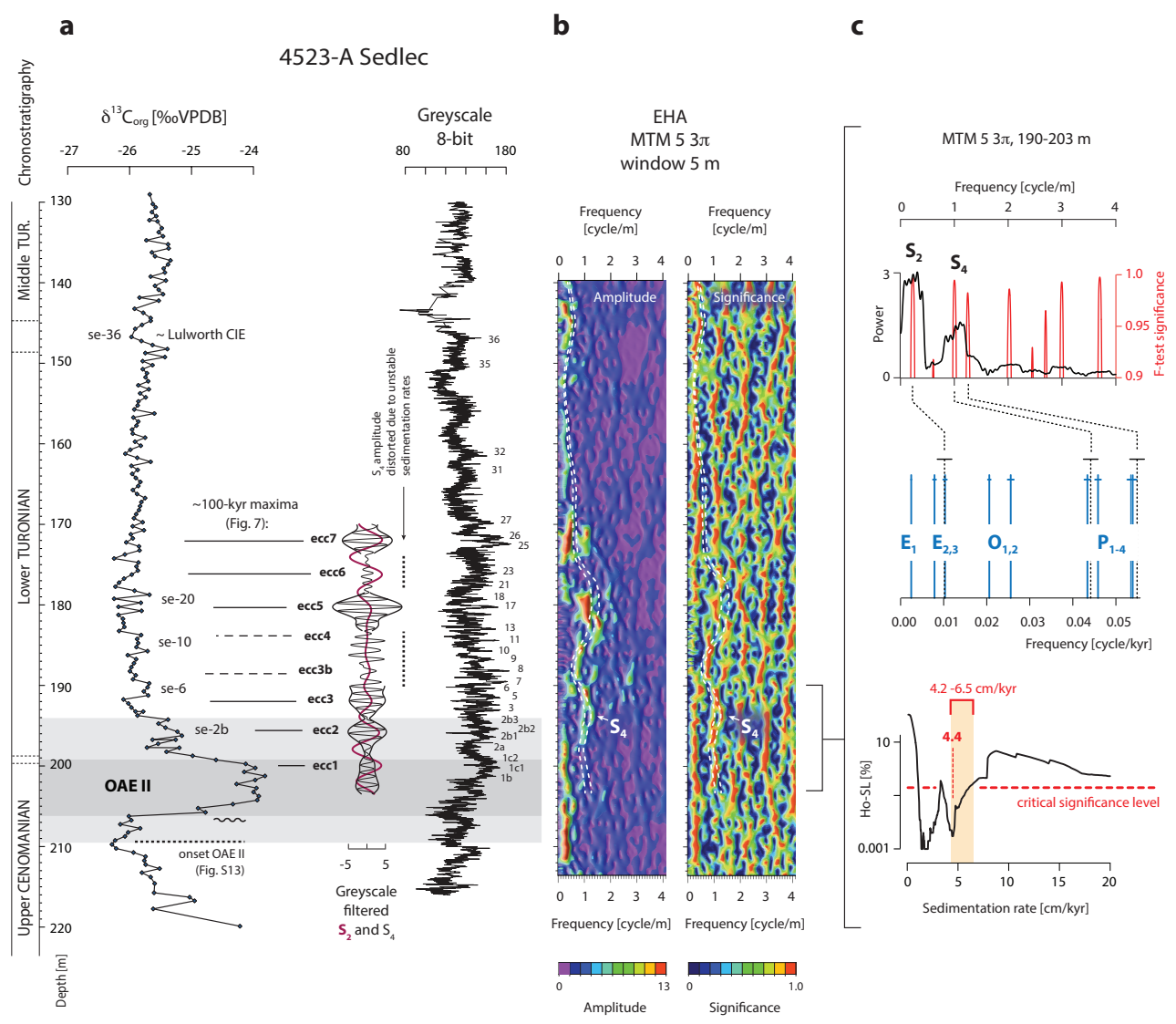
a
4523-A Sedlec
Chronostratigraphy
δ13Corg [‰VPDB]
-27
-26
-25
-24
Greyscale
8-bit
80
180
Middle TUR.
Lower TURONIAN
Upper CENOMANIAN
130
140
150
160
170
180
190
200
210
220
Depth [m]
se-36
~ Lulworth CIE
~100-kyr maxima
(Fig. 7):
ecc7
ecc6
se-20
ecc5
se-10
ecc4
ecc3b
se-6
ecc3
se-2b
ecc2
ecc1
OAE II
onset OAE II
(Fig. S13)
S4 amplitude
distorted due to unstable
sedimentation rates
-5
5
Greyscale
filtered
S2 and S4
b
EHA
MTM 5 3π
window 5 m
Frequency
[cycle/m]
0
1
2
3
4
Amplitude
Significance
S4
Frequency [cycle/m]
0
13
Amplitude
0
1.0
Significance
c
MTM 5 3π, 190-203 m
Frequency [cycle/m]
S2
S4
Power
3
0
1.0
0.95
0.9
F-test significance
E1
E2,3
O1,2
P1-4
0.00
0.01
0.02
0.03
0.04
0.05
Frequency [cycle/kyr]
4.2 -6.5 cm/kyr
4.4
10
0.001
Ho-SL [%]
critical significance level
0
5
10
15
20
Sedimentation rate [cm/kyr]

Figure 7.

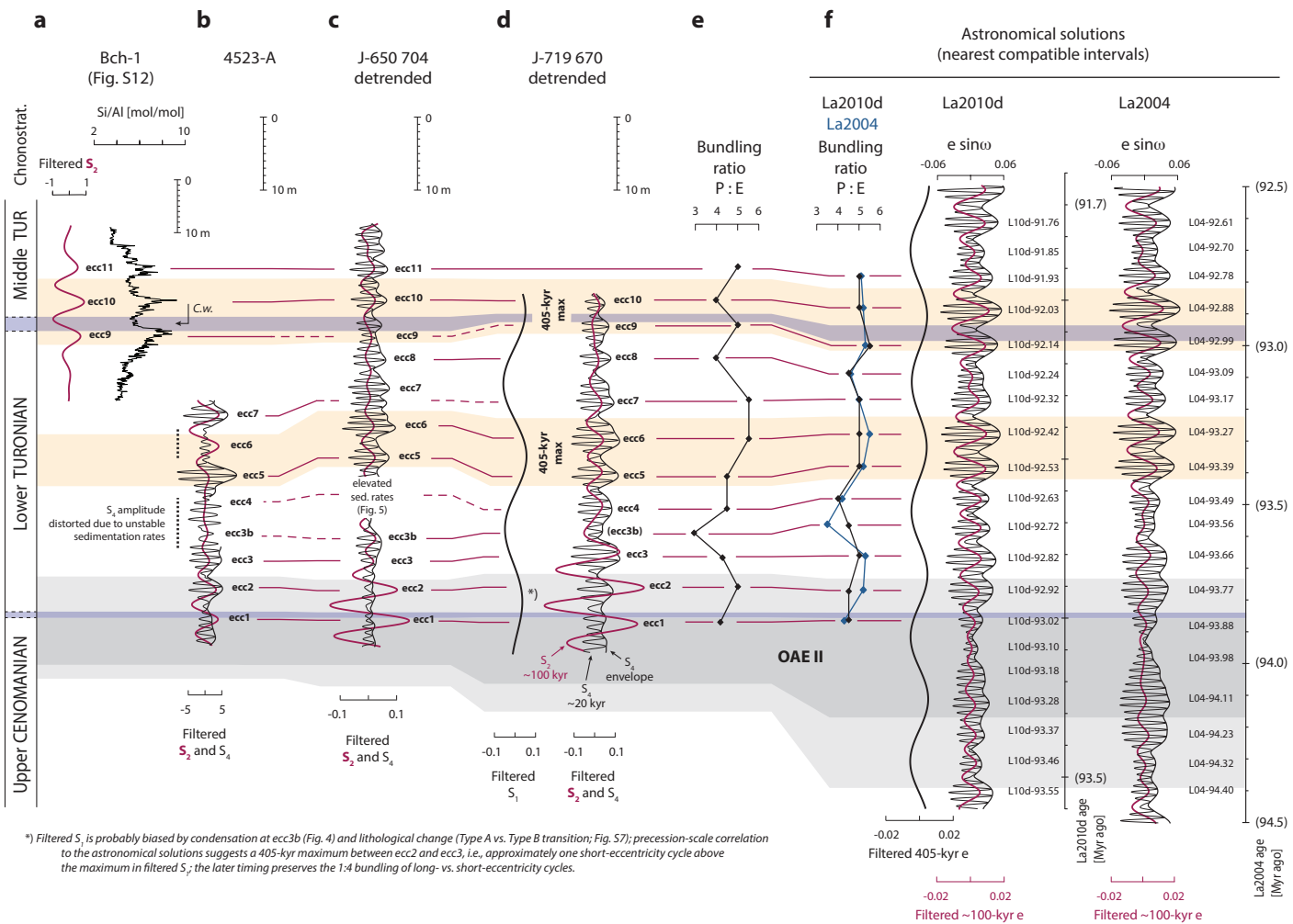

*) *Filtered S_1 is probably biased by condensation at ecc3b (Fig. 4) and lithological change (Type A vs. Type B transition; Fig. S7); precession-scale correlation to the astronomical solutions suggests a 405-kyr maximum between ecc2 and ecc3, i.e., approximately one short-eccentricity cycle above the maximum in filtered S_1; the later timing preserves the 1:4 bundling of long- vs. short-eccentricity cycles.*

Figure 8.

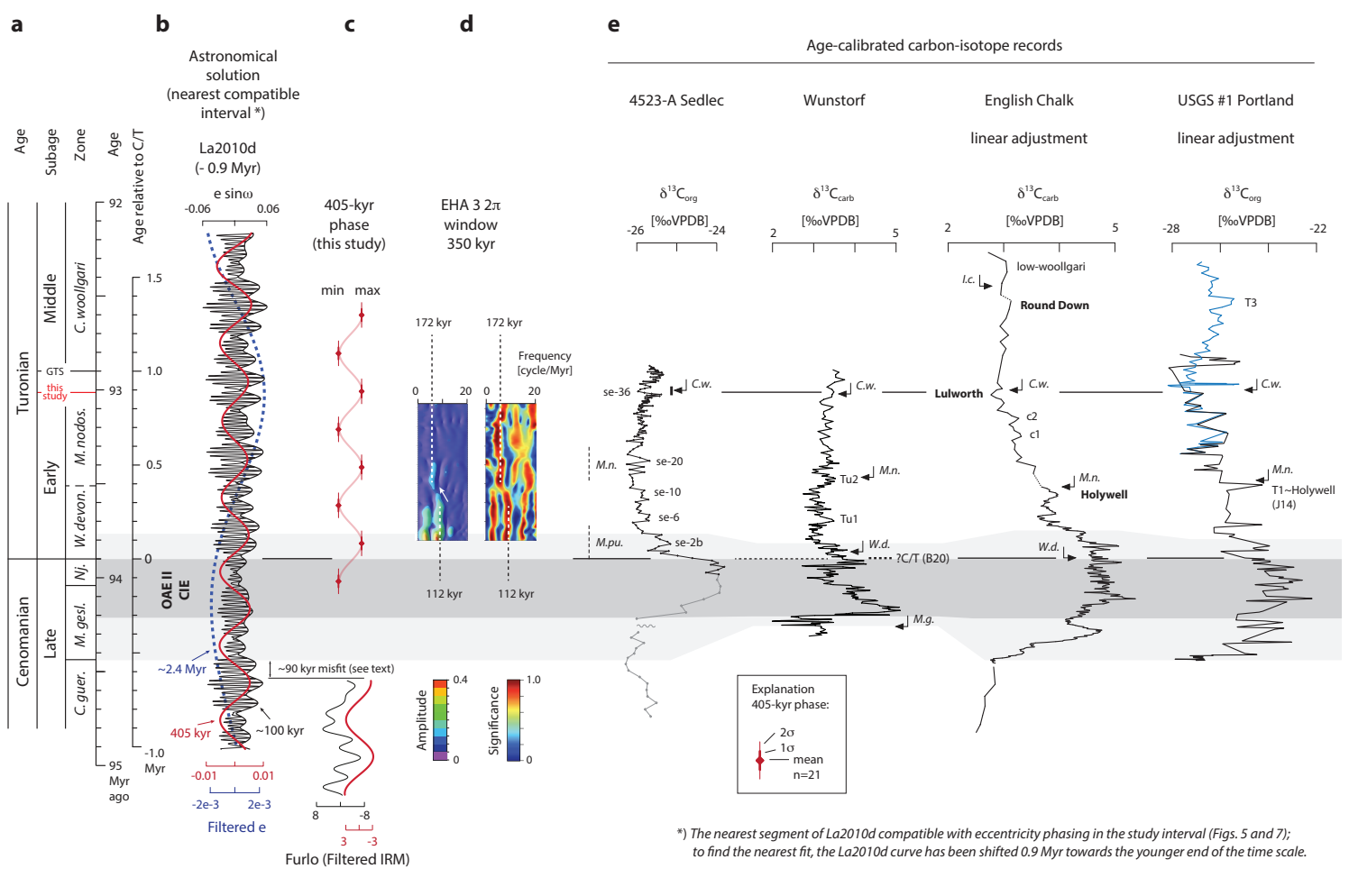

*) *The nearest segment of La2010d compatible with eccentricity phasing in the study interval (Figs. 5 and 7); to find the nearest fit, the La2010d curve has been shifted 0.9 Myr towards the younger end of the time scale.*